

# A Comparison of 2D Magnetohydrodynamic Supernova Simulations with the CoCoNuT-FMT and AENUS-ALCAR Codes

Vishnu Varma,<sup>1\*</sup> Bernhard Müller<sup>1†</sup> and Martin Obergaulinger<sup>2</sup>

<sup>1</sup>*School of Physics and Astronomy, 19 Rainforest Walk, Monash University, VIC 3800, Australia*

<sup>2</sup>*Departament d'Astronomia i Astrofísica, Universitat de València, Edifici d'Investigació Jeroni Munyoz, C/Dr. Moliner, 50, E-46100 Burjassot (València), Spain*

Accepted XXX. Received YYY; in original form ZZZ

## ABSTRACT

Code comparisons are a valuable tool for the verification of supernova simulation codes and the quantification of model uncertainties. Here we present a first comparison of axisymmetric magnetohydrodynamic (MHD) supernova simulations with the CoCoNuT-FMT and AENUS-ALCAR codes, which use distinct methods for treating the MHD induction equation and the neutrino transport. We run two sets of simulations of a rapidly rotating  $35M_{\odot}$  gamma-ray burst progenitor model with different choices for the initial field strength, namely  $10^{12}$  G for the maximum poloidal and toroidal field in the strong-field case and  $10^{10}$  G in the weak-field case. We also investigate the influence of the Riemann solver and the resolution in CoCoNuT-FMT. The dynamics is qualitatively similar for both codes and robust with respect to these numerical details, with a rapid magnetorotational explosion in the strong-field case and a delayed neutrino-driven explosion in the weak-field case. Despite relatively similar shock trajectories, we find sizeable differences in many other global metrics of the dynamics, like the explosion energy and the magnetic energy of the proto-neutron star. Further differences emerge upon closer inspection, for example, the disk-like surface structure of the proto-neutron star proves highly sensitive to numerical details. The electron fraction distribution in the ejecta as a crucial determinant for the nucleosynthesis is qualitatively robust, but the extent of neutron- or proton-rich tails is sensitive to numerical details. Due to the complexity of the dynamics, the ultimate cause of model differences can rarely be uniquely identified, but our comparison helps gauge uncertainties inherent in current MHD supernova simulations.

**Key words:** supernovae: general – MHD – methods: numerical

## 1 INTRODUCTION

It was first recognised by [Baade & Zwicky \(1934\)](#) that in supernova explosions of massive stars ( $\geq 8M_{\odot}$ ) a small fraction of the energy released during the terminal collapse of the stellar iron core is somehow transferred to the stellar envelope to produce a powerful explosion known as a core-collapse supernova (CCSN). The ensuing quest for the details of the explosion mechanism has been ongoing for decades. Among the many suggested explosion scenarios, the neutrino-driven mechanism, initially proposed by [Colgate & White \(1966\)](#) has emerged as the favoured explanation for the majority of CCSN explosions. In the modern paradigm of the delayed neutrino-driven mechanism ([Bethe & Wilson 1985](#)), shock revival is accomplished thanks to the increase of the post-shock pressure due to partial reabsorption of neutrinos that stream out from the young proto-neutron star (PNS) and the cooling layer of accreted material on its surface. Detailed simulations have determined that additional support by multi-dimensional instabilities like turbulent convection ([Herant 1995](#); [Burrows et al. 1995](#)) and the standing accretion shock instability ([Blondin et al. 2003](#)) is critical to make the neutrino-driven mechanism work.

Partly due to increasing computing power, supernova simulations have been able to continually include more detailed physics such as multi-group neutrino transport, magnetic fields, and general relativity, and to abandon symmetry assumptions in favour of fully three-dimensional models, but even the most sophisticated simulations still need to make approximations (for recent reviews, see [Janka 2012](#); [Burrows 2013](#); [Müller 2016, 2020](#); [Mezzacappa et al. 2020](#)). The complexity of the codes and the disparities in numerical methodology present a challenge for drawing robust conclusions on the workings of the supernova engine from the models. Code comparison studies are a useful approach for increasing the robustness and reliability of simulation results and have already addressed many important ingredients of supernova codes, some focusing more strictly on the neutrino transport (e.g. [Yamada et al. 1999](#); [Ott et al. 2008](#); [Richers et al. 2017](#); [Chan et al. 2020](#)), whereas others have more broadly addressed the interplay of neutrino transport and hydrodynamics in 1D, 2D ([Liebendörfer et al. 2005](#); [Müller et al. 2010](#); [O'Connor et al. 2018](#); [Just et al. 2018](#)) and to some extent in 3D ([Cabezón et al. 2018](#)) with different solvers for the hydrodynamics and the neutrino transport alike. Numerical uncertainties related to the effects of grid resolution have also received considerable attention (e.g., [Abdikamalov et al. 2015](#); [Handy et al. 2014](#); [Hanke et al. 2013](#); [Couch & O'Connor 2014](#); [Radice et al. 2016](#); [Nagakura et al. 2019](#); [Melson et al. 2020](#)).

\* E-mail: vishnu.rvejayan@monash.edu

† E-mail: bernhard.mueller@monash.edu

A similarly broad exploration of numerical uncertainties is yet to be performed for magnetorotational explosions, which constitute the best-explored alternative to the neutrino-driven mechanism and are widely thought to operate in hyperenergetic supernovae (“hypernovae”), some of which are also associated with long gamma ray bursts (GRBs; [Woodsley & Bloom 2006](#)). In this scenario, whose history can be traced to early pioneering work of [LeBlanc & Wilson \(1970\)](#); [Bisnovaty-Kogan et al. \(1976\)](#); [Meier et al. \(1976\)](#); [Müller & Hillebrandt \(1979\)](#), rapid rotation and strong magnetic fields are the critical ingredients for the explosion; the magnetic fields help tap the rotational energy of the forming compact object and channel it into kinetic energy in outflows – usually in the form of collimated, magnetically-dominated jets – which are driven either by magnetic forces and pressure or through viscous heating behind the shock.

With the inclusion of rotation and magnetic fields in models, many additional unknowns enter into the simulations and have received substantial attention. The magnetorotational explosion mechanism is intimately linked to the problem of rotation and magnetism in massive stars. Initial conditions for magnetorotational explosion simulations currently come from “1.5D” stellar evolution models that assume shellular rotation and include effective recipes for magnetic field generation and angular momentum transport by hydrodynamic and magnetohydrodynamic processes ([Heger et al. 2000, 2005](#); [Woodsley & Heger 2006](#)). Efforts to better understand the angular momentum distribution and magnetic fields in the cores of massive stars by means of multi-dimensional simulation have only started recently ([Varma & Müller 2021](#); [Yoshida et al. 2021](#); [McNeill & Müller 2021](#)). Since 1.5D stellar evolution models predict magnetic fields that are rather weak and predominantly toroidal, the general notion has long been that field amplification processes after collapse are critical in magnetorotational explosions, although this has recently been challenged ([Obergaullinger & Aloy 2017, 2021](#); [Aloy & Obergaullinger 2021](#)). These amplification processes have duly received considerable attention. [Akiyama et al. \(2003\)](#) pointed out the potential importance of the magnetorotational instability (MRI; [Balbus & Hawley 1991](#)), which has been addressed in the context of CCSNe in a host of numerical and analytic studies ([Obergaullinger et al. 2009](#); [Sawai et al. 2013](#); [Sawai & Yamada 2016](#); [Masada et al. 2015](#); [Guilet & Müller 2015](#); [Guilet et al. 2015](#); [Mösta et al. 2015](#); [Rembiasz et al. 2016a,b](#); [Reboul-Salze et al. 2021](#)). Field amplification by an  $\alpha$ - $\Omega$  dynamo in the PNS ([Thompson & Duncan 1993](#)) has also been investigated in multi-D simulations as an avenue for generating strong magnetic fields on large scales from weak seed fields ([Raynaud et al. 2020](#)). While important issues like the initial fields and angular momentum distribution, the saturation of the MRI, and non-ideal effects still warrant further investigation, global simulations of magnetorotational explosions based on parameterised initial fields have been available for quite some time in 2D both with ([Burrows et al. 2007](#); [Dessart et al. 2007](#); [Obergaullinger & Aloy 2017, 2020](#); [Bugli et al. 2020](#); [Aloy & Obergaullinger 2021](#); [Jardine et al. 2021](#)) and without ([Kotake et al. 2004](#); [Takiwaki et al. 2004](#); [Sawai et al. 2005](#); [Obergaullinger et al. 2006](#); [Moiseenko et al. 2006](#); [Takiwaki et al. 2009](#)) detailed neutrino transport, and are becoming routine in 3D ([Winteler et al. 2012](#); [Mösta et al. 2014, 2018](#); [Halevi & Mösta 2018](#)), even though only few models ([Kuroda et al. 2020](#); [Obergaullinger & Aloy 2021](#); [Bugli et al. 2021](#)) also include neutrino transport.

As magnetohydrodynamic supernova simulations mature and are being used to understand hypernova light curves ([Shankar et al. 2021](#)) and explosion properties and the potential role of hypernovae as a site for the rapid-neutron capture process ([Winteler et al. 2012](#); [Mösta et al. 2018](#); [Reichert et al. 2021](#)), it is critical to better address numerical uncertainties in these models following a similar approach

as for neutrino-driven explosions, where comparison studies with different codes and resolutions studies have done much to distinguish between robust and uncertain features of the mechanism. However, to date, no study has as yet compared simulations of magnetorotational supernovae using independent codes.

In this paper, we present the first comparison of axisymmetric (2D) magnetorotational explosions simulations between two independent codes, namely the CoCoNuT-FMT ([Müller & Janka 2015](#); [Müller & Varma 2020](#)) and AENUS-ALCAR ([Obergaullinger 2008](#); [Obergaullinger et al. 2014](#)) codes. We also conduct a minimal resolution study with CoCoNuT-FMT models and explore the sensitivity of the results to the approximate Riemann solver. Our paper is organised as follows: In Section 2, we describe the magnetohydrodynamic (MHD) solvers in CoCoNuT-FMT and AENUS-ALCAR and also provide a brief description of the neutrino transport schemes. We then outline the simulation setup in Section 3. We compare the CoCoNuT-FMT and AENUS-ALCAR results in Section 4 and present results for our minimal resolution study with CoCoNuT-FMT in Section 5. We conclude with a summary and evaluation in Section 6.

## 2 NUMERICAL METHODS

We perform axisymmetric core-collapse supernova simulations with the pseudo-Newtonian MHD version of CoCoNuT-FMT ([Müller et al. 2010](#); [Müller & Janka 2015](#)) and the special relativistic AENUS-ALCAR code ([Obergaullinger 2008](#); [Just et al. 2015](#)). In both codes, we use an effective gravitational potential (Case A from [Marek et al. 2006](#)) to approximately capture general relativistic effects. The nuclear equation of state of [Lattimer & Swesty \(1991\)](#) with an incompressibility of  $K = 220$  MeV is used for all models at high densities. Here we briefly outline the magnetohydrodynamic and neutrino transport solvers in the two codes. For more details, we refer to the relevant code papers.

### 2.1 CoCoNuT-FMT Code

The CoCoNuT-FMT supernova code is built on a Godunov-based finite-volume solver for spherical polar coordinates that uses higher-order reconstruction ([Colella & Woodward 1984](#); [Colella & Sekora 2008](#)). It has recently been upgraded to solve the Newtonian MHD equations ([Müller & Varma 2020](#)) using the HLLC Riemann solver ([Gurski 2001](#); [Miyoshi & Kusano 2005](#)), and the divergence free condition  $\nabla \cdot \mathbf{B} = 0$  is maintained using a variant of hyperbolic divergence cleaning introduced in [Dedner et al. \(2002\)](#). This method involves introducing an additional scalar field,  $\psi$ , known as a generalized Lagrange multiplier, which couples to the induction equation and propagates the divergence errors at a cleaning speed  $c_h$  to the domain boundaries. We apply a modification of hyperbolic divergence cleaning that allows for variable cleaning speeds following the ideas of [Tricco et al. \(2016\)](#) for increased stability. Compared to the original cleaning method, we instead propagate a modified scalar field,  $\hat{\psi} = \psi/c_h$ , where the cleaning speed  $c_h$  is chosen as one fourth of the maximum local signal speed allowed by the Courant-Friedrichs-Lewy limit (which is different from [Müller & Varma 2020](#), where the cleaning speed was set to the fast magnetosonic wave speed). The extended system of MHD equations for the density  $\rho$ , velocity  $\mathbf{v}$ , magnetic field  $\mathbf{B}$ , the total energy density  $e$ , and the Lagrange

multiplier  $\hat{\psi}$  reads,

$$\partial_t \rho + \nabla \cdot \rho \mathbf{v} = 0, \quad (1)$$

$$\partial_t (\rho \mathbf{v}) + \nabla \cdot \left( \rho \mathbf{v} \mathbf{v} - \frac{\mathbf{B}\mathbf{B}}{4\pi} + P_t \mathcal{I} \right) = \rho \mathbf{g} - \frac{(\nabla \cdot \mathbf{B})\mathbf{B}}{4\pi} + \mathbf{Q}_m, \quad (2)$$

$$\partial_t e + \nabla \cdot \left[ (e + P_t) \mathbf{u} - \frac{\mathbf{B}(\mathbf{v} \cdot \mathbf{B})}{4\pi} \right] = \rho \mathbf{g} \cdot \mathbf{v} + Q_e + \mathbf{Q}_m \cdot \mathbf{v} - \mathbf{B} \cdot \nabla (c_h \hat{\psi}), \quad (3)$$

$$\partial_t \mathbf{B} + \nabla \cdot (\mathbf{v}\mathbf{B} - \mathbf{B}\mathbf{v}) + \nabla (c_h \hat{\psi}) = 0 \quad (4)$$

$$\partial_t \hat{\psi} + c_h \nabla \cdot \mathbf{B} = -\hat{\psi}/\tau. \quad (5)$$

where  $\mathbf{g}$  is the gravitational acceleration,  $P_t$  is the total pressure,  $\mathcal{I}$  is the Kronecker tensor,  $c_h$  is the hyperbolic cleaning speed,  $\tau$  is the damping timescale for divergence cleaning. The neutrino energy and momentum source terms are denoted by  $Q_e$  and  $\mathbf{Q}_m$ . Different from Müller & Varma (2020), the total energy density  $e$  does not contain the cleaning field and is given by its standard definition,

$$e = \rho \left( \epsilon + \frac{v^2}{2} \right) + \frac{B^2}{8\pi}, \quad (6)$$

where  $\epsilon$  is the mass-specific internal energy.

In the CoCoNuT models the innermost 10 km are treated in 1D to avoid an overly stringent Courant time step limit near the origin of the grid. The thermodynamic variables and the radial velocity are assumed to be spherically symmetric. The non-radial velocity components and the magnetic fields are not set to zero in the core, however. Instead, we assume uniform rotation at a rate corresponding to the total angular momentum in the core, and the magnetic field in the core is represented by vector spherical harmonics of degree  $\ell = 1$ , whose coefficients are evolved according to the induction equation.

The fast multi-group transport (FMT) scheme of Müller & Janka (2015) is used for the neutrino transport. The FMT scheme solves the energy-dependent stationary zeroth-momentum equation using a hybrid closure based on a two-stream Boltzmann solution and an analytic Eddington closure at flux factors  $h > 0.5$ . The scheme accounts for gravitational redshift, but mostly disregards velocity-dependent terms, except for an effective frame correction of the absorption opacity at low optical depth (Müller et al. 2019). The set of neutrino rates includes emission by and absorption on nucleons and nuclei, neutrino scattering on nucleons and nuclei, and, for heavy-flavour neutrinos, Bremsstrahlung in an effective one-particle approximation. Recoil energy transfer in neutrino-nucleon scattering is included approximately. Nucleon potentials are taken into account in charged-current neutrino-nucleon interactions (Martínez-Pinedo et al. 2012). Nucleon correlations are included following Horowitz et al. (2017). Neutral-current scattering cross sections are computed following Horowitz (2002) with a somewhat large value for the nucleon strangeness of  $g_A = -0.1$ . The deleptonisation scheme of Liebendörfer (2005) is used during the collapse phase.

## 2.2 AENUS-ALCAR Code

The AENUS-ALCAR code solves the special relativistic version of the MHD equations. Different from CoCoNuT, the divergence constraint is accounted for by using a constrained transport scheme (Evans & Hawley 1988). The equations of MHD are also solved using the HLLC solver, but combined with MP5 reconstruction (Suresh & Huynh 1997). The code can accommodate different coordinate systems, but is also run in spherical polar coordinates in this study.

AENUS-ALCAR treats the innermost 10 km in 2D, but with a coarser grid resolution.

Neutrinos are treated by a spectral scheme for two-moment transport with an analytic closure (see Just et al. 2015, for an overview). Neutrinos of different energies are coupled via the effects of Doppler shifts, aberration, and gravitational redshift treated to  $\mathcal{O}(v/c)$ . The set of reactions included in the AENUS-ALCAR simulations is given in detail in, e.g., Obergaulinger & Aloy (2017); Obergaulinger et al. (2018) and consists of emission/absorption and scattering reactions with nucleons and nuclei, inelastic scattering off electrons, electron-positron annihilation, and nucleon-nucleon Bremsstrahlung.

We do not aim to reproduce perfectly identical neutrino microphysics in both codes. We rather pit the two codes against each other as used in normal production runs so that the comparison is more reflective of “real-life” uncertainties encountered in magnetorotational supernovae. To give a conservative assessment of possible errors, we view it as one useful strategy to overestimate rather than to underestimate code differences by not making the models more similar than they would be in independent studies. Of course, this also entails some risk of accidental error cancellation in some (but not all) metrics of the code comparison. This strategy is complementary to the opposite approach of reproducing all of the physics as closely as possible in different codes, which will be a useful undertaking for the future, perhaps within a comparison broader with a broader community base.

## 3 MODEL SETUP

All our simulations use the stellar progenitor model 35OC of Woosley & Heger (2006). This model was computed using the KEPLER code including a prescription for angular momentum transport by magnetic torques (Spruit 2002; Heger et al. 2005). The 35OC stellar model is a rapidly rotating model with an initial total angular momentum of  $J_{\text{init}} = 10^{52}$  erg s and a surface rotational velocity  $v_{\text{rot}} = 380$  km/s on the zero-age main sequence (ZAMS). The progenitor has a ZAMS mass of  $M_{\text{ZAMS}} = 35M_{\odot}$ , but at the time of core collapse mass loss has reduced its total mass to  $M_{\text{final}} = 28.07M_{\odot}$ .

We set up our models using the shellular rotation profile of the progenitor, but modify the original magnetic fields of the 35OC model to similar initial conditions as in models 35OC-Rs (strong field) and 35OC-Rw (weak field) from Obergaulinger & Aloy (2017). Strong field models are set up with an initial maximum poloidal and toroidal magnetic field of  $B_{\text{pol,tor}} = 10^{12}$  G and weak field cases have  $B_{\text{pol,tor}} = 10^{10}$  G. Throughout the rest of this paper, references to the strong-field models will include a suffix “-Rs” while the weak-field models will have a suffix “-Rw” to the model names. The magnetic field geometry in either case is defined using the vector potential  $\mathbf{A}$  from Suwa et al. (2007),

$$(A^r, A^\theta, A^\phi) = \frac{1}{2(r^3 + r_0^3)} \left( B_{\text{tor}} r_0^3 r \cos \theta, 0, B_{\text{pol}} r_0^3 r \sin \theta \right), \quad (7)$$

where the radius parameter is set to  $r_0 = 10^8$  cm.<sup>1</sup>

All the CoCoNuT-FMT models (denoted by a prefix “coco”) have a computational domain that extends out to  $R_{\text{out}} = 10^5$  km using a nonuniform radial grid of 550 zones and spans colatitudes  $\theta$  in the

<sup>1</sup> Note that models 35OC-Rs and 35OC-Rw in Obergaulinger & Aloy (2017) had inadvertently used a slightly different radial dependence for the toroidal field, which is why ALCAR models were rerun with the exact initial conditions given in Equation (7).

range  $[0^\circ, 180^\circ]$  on a spherical polar grid with 128 zones in  $\theta$ . The AENUS-ALCAR models (denoted by a prefix “Alcar”) implement the same angular resolution, but have a computational domain of 400 radial zones that extends to  $R_{\text{out}} = 1.4 \times 10^5$  km.

We simulate three pairs of models with CoCoNuT-FMT. For each strong- and weak-field model, we conduct runs using the MHD version of the HLLC Riemann solver (Gurski 2001) or the HLLC solver (Einfeldt 1988). These runs are labelled as coco-HLLC-Rs/w and coco-HLLE-Rs/w, respectively. In addition, we conduct two high-resolution runs coco-Res-Rs/w with the HLLC solver with 256 zones in angle for a minimal resolution test. The parameters of all runs are summarised in Table 1.

## 4 RESULTS – CODE COMPARISON

In the following, we present a comparison of the standard resolution models coco-HLLC-Rs, coco-HLLC-Rw, coco-HLLE-Rs and coco-HLLE-Rw to models Alcar-Rs and Alcar-Rw as described in Table 1. We discuss the differences between the AENUS-ALCAR and CoCoNuT-FMT results, as well as between the HLLC and HLLC Riemann solvers implemented in CoCoNuT-FMT.

### 4.1 Shock Propagation

We begin by comparing the propagation of the shock (Figure 1) between the different models as this is one of the most basic metrics for the post-bounce dynamics. Due to the strong asymmetry of the explosion, the dynamics is best captured by the maximum shock radius rather than the angle-averaged shock radius, especially in the case of the strong magnetic field models, which develop a veritable jet-driven explosion with strongly collimated polar outflows.

In Alcar-Rs, shock expansion starts promptly after core bounce and does not exhibit a stalled shock phase. By contrast, both coco-HLLC-Rs and coco-HLLE-Rs stall for a short period of  $\approx 50$  ms before the shock is revived. After shock revival, the shock in models coco-HLLC-Rs and coco-HLLE-Rs expands rapidly, achieving similar maximum shock radii as Alcar-Rs at the end of the simulations.

The different time of explosion in ALCAR and CoCoNuT may be due to different dynamics of magnetic field amplification in the PNS surface region that result in the earlier emergence of a jet in model Alcar-Rs. There may, however, be a compounding factor in the form of the collapse dynamics. Both in the strong-field case and the weak-field case, the Alcar models take 30–35 ms longer to collapse. The mass accretion rate at 45–130 ms differs noticeably between CoCoNuT and ALCAR with CoCoNuT exhibiting higher mass accretion rates early on after collapse (Figure 2). The collapse time is known to be sensitive to the microphysics (Hüdepohl 2014; Powell et al. 2021), and although both codes use the same high-density equation of state, they differ in their treatment of the low-density equation of state, nuclear burning, and deleptonisation during collapse. Factors that affect the collapse dynamics may be exacerbated by transient adjustment of the stellar models after mapping the 1D stellar evolution model with shellular rotation into the supernova simulation codes. Although the resulting difference of the infall dynamics are mostly confined to the collapse phase, it is known that differences in the mass accretion rate can persist for some time after collapse even in simulations of non-rotating progenitors (Hüdepohl 2014). In the subsequent analysis, one must bear in mind that this will inevitably impact the shock propagation as well as the evolution of the PNS properties, and, more importantly, the neutrino emission at early post-bounce times to some degree.

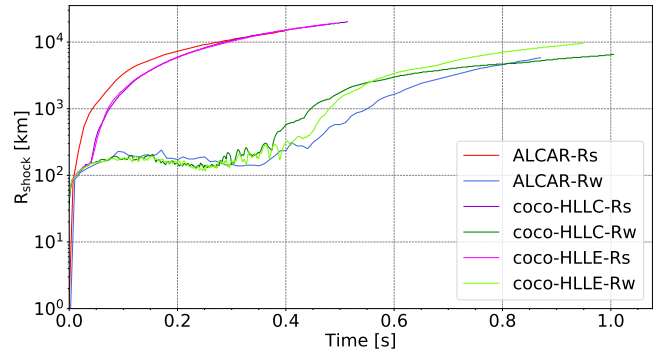


**Figure 1.** Evolution of the maximum shock radius at standard resolution for CoCoNuT-FMT using the HLLC and HLLC Riemann solver models along with the AENUS-ALCAR models. Both the strong-field (-Rs) and weak-field (-Rw) models are shown.

Unlike the strong-field models, the models with weaker magnetic fields (coco-HLLC-Rw, coco-HLLE-Rw, Alcar-Rw) all go through a prolonged accretion phase, similar to the dynamics in purely neutrino-driven explosions of massive progenitors. The shock trajectories during the accretion phase are similar, with Alcar-Rw exhibiting slightly larger stalled shock radii early on, but slightly slower shock expansion later. Most of the time, the relative difference between the runs remains below 10%. All three models undergo shock revival around 0.4 s post-bounce with minor differences. The Alcar-Rw model is the last to explode and continues to have a smaller shock radius than both CoCoNuT-FMT models until about 0.8 s where its shock radii slightly surpasses that of coco-HLLC-Rw. At their largest divergence, the relative difference between the three models is  $\approx 12\%$ . We also note that the CoCoNuT-FMT weak-field models show a much more pronounced and prolonged activity of the standing accretion shock instability (SASI; Blondin et al. 2003; Fogliizzo et al. 2007; Guilet & Fogliizzo 2012, visible as oscillations in the maximum shock radius in coco-HLLC-Rw and coco-HLLE-Rw in the phase leading up to shock revival. This is in line with the established finding that stronger shock retraction is conducive to more vigorous SASI activity (Scheck et al. 2008; Müller et al. 2012).

Shock revival in model coco-HLLE-Rw occurs about 0.05s later than in model coco-HLLC-Rw, but the shock subsequently expands faster than in the HLLC model, exhibiting a larger maximum shock radius at the end of the simulation runs. By contrast, no significant differences are seen between coco-HLLE-Rs and coco-HLLC-Rs. Since shock trajectories differ between the HLLC and HLLC run only in the weak-field case, which develops a “hybrid” explosion supported alike by magnetic fields, neutrino heating, and convection (Obergaullinger & Aloy 2017), we suspect the differences between coco-HLLE-Rw and coco-HLLC-Rw do not actually reflect a systematic dependence on the Riemann solver, but are due to stochastic variations, which have been shown to be considerable in explosion models without MHD in 2D (Müller 2015; Cardall & Budiardja 2015).

Overall, the differences in shock propagation between the corresponding CoCoNuT-FMT and AENUS-ALCAR models are within the range of deviations between independent codes in comparisons of neutrino hydrodynamics simulations in 2D (Müller & Janka 2015; Cabezón et al. 2018; Just et al. 2018). Even in controlled 1D comparisons with identical neutrino rates (Liebendörfer et al. 2005; Müller et al. 2010; O’Connor et al. 2018), deviations of the order of 10–20% in shock radius are not uncommon. We suspect that the prompt ex-



Model	Riemann solver	Resolution	Maximum initial field $B_{\text{pol}}, B_{\text{tor}}$	Time of bounce	Final simulation time	Explosion Energy
Alcar-Rs	HLLC	$400 \times 128$ zones	$10^{12}$ G	0.433 s	0.397 s	$1.27 \times 10^{51}$ erg
Alcar-Rw	HLLC	$400 \times 128$ zones	$10^{10}$ G	0.430 s	0.870 s	$1.11 \times 10^{50}$ erg
coco-HLLC-Rs	HLLC	$550 \times 128$ zones	$10^{12}$ G	0.396 s	0.516 s	$7.71 \times 10^{50}$ erg
coco-HLLC-Rw	HLLC	$550 \times 128$ zones	$10^{10}$ G	0.396 s	1.005 s	$2.42 \times 10^{50}$ erg
coco-HLLE-Rs	HLLE	$550 \times 128$ zones	$10^{12}$ G	0.395 s	0.482 s	$6.69 \times 10^{50}$ erg
coco-HLLE-Rw	HLLE	$550 \times 128$ zones	$10^{10}$ G	0.395 s	0.948 s	$5.19 \times 10^{50}$ erg
coco-Res-Rs	HLLC	$550 \times 256$ zones	$10^{12}$ G	0.396 s	0.434 s	$5.49 \times 10^{50}$ erg
coco-Res-Rw	HLLC	$550 \times 256$ zones	$10^{10}$ G	0.396 s	0.924 s	$2.09 \times 10^{50}$ erg

**Table 1.** Overview of the eight models included in the comparison, summarising the setup (code, Riemann solver, resolution, initial magnetic field strength) as well as the time of bounce, the final post-bounce simulation time, and the explosion energy for each run, recorded at  $\approx 0.85$  s for the weak-field models (“-Rw”) and at  $\approx 0.39$  s for the strong-field models (“-Rs”). Riemann solvers and resolution of all models run on CoCoNuT and the ones run with AENUS-ALCAR.

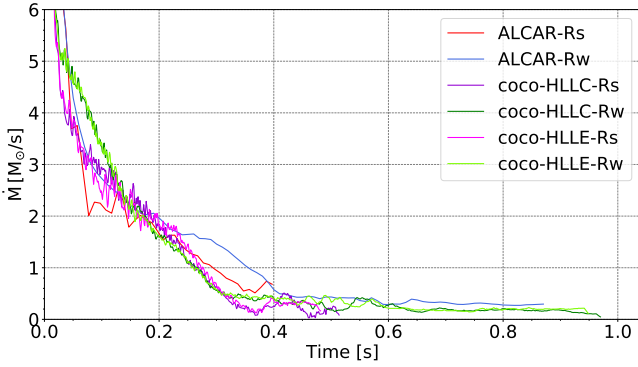


**Figure 2.** Mass accretion rate  $\dot{M}$  as a function of post-bounce time, measured as the time derivative of the mass of the PNS (defined as the region where  $\rho > 10^{11} \text{ g cm}^{-3}$ ).

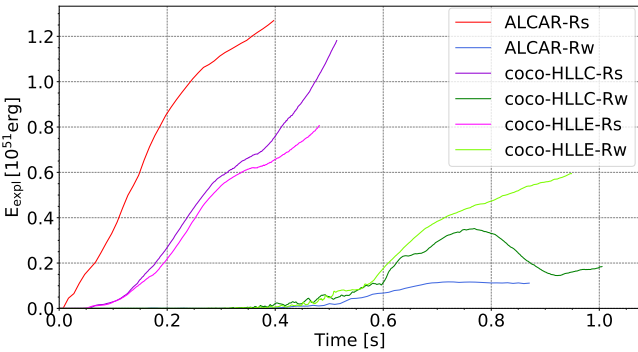


**Figure 3.** Evolution of the diagnostic explosion energy  $E_{\text{expl}}$  for CoCoNuT-FMT and AENUS-ALCAR models with strong and weak initial magnetic fields.

plosion in Alcar-Rs that is not mirrored in the strong magnetic field models of CoCoNuT-FMT is an artefact of the different treatments of the inner core. As described in Section 3, AENUS-ALCAR treats the inner core in coarse 2D geometry, which allows for rotational shear and hence more rapid magnetic field amplification immediately after bounce, and consequently, larger magnetic pressure to immediately drive the shock out. These difference in magnetic field amplification will be discussed further in Section 4.3.

## 4.2 Explosion Energetics

As the next metric of comparison for the global dynamics, we consider the diagnostic explosion energy  $E_{\text{expl}}$  (Buras et al. 2006). The diagnostic explosion energy is defined as an integral over the region that is nominally unbound,

$$E_{\text{expl}} = \int_{e_{\text{tot}} > 0} \rho e_{\text{tot}} dV, \quad (8)$$

where  $e_{\text{tot}}$  is the total energy density, i.e., the sum of the internal, kinetic, gravitational, and magnetic energy density (the latter of which was not included in Buras et al. 2006). The evolution of the diagnostic explosion energy  $E_{\text{expl}}$  is shown for all models in Figure 3. The strong magnetic field models exhibit a very quick rise in explosion energy following the early and rapid expansion of the shock, whereas the weak-field models develop positive  $E_{\text{expl}}$  at  $\sim 400$  ms after bounce, and remain below  $10^{51}$  erg in explosion energy.

Although the CoCoNuT-FMT and AENUS-ALCAR models show qualitative agreement in the evolution of  $E_{\text{expl}}$ , Figure 3 more clearly exhibits quantitative differences between the runs than could be seen in the shock propagation. Among the strong-field models, models coco-HLLE-Rs and coco-HLLC-Rs agree quite well with each other, but develop a positive diagnostic energy later than the Alcar-Rs run, which is consistent with the longer delay to shock revival discussed in the previous section. After this slight delay, model coco-HLLC-Rs in particular exhibits comparable rates of explosion energy growth, with Alcar-Rs increasing at  $\approx 3.12 \times 10^{51} \text{ erg s}^{-1}$  while model coco-HLLC-Rs shows, on average, a rise at a rate of  $\approx 3.17 \times 10^{51} \text{ erg s}^{-1}$ . The explosion in coco-HLLE-Rs initially grows at a similar rate as in coco-HLLC-Rs, but the model becomes slightly less energetic by the end of the simulation. The cause of this divergence is unclear but since our simulations end by 500 ms, it is possible that this is just a temporary deviation due to some element of stochasticity in the dynamics of the evolving explosion. The diagnostic energy is evidently a much more sensitive measure for the dynamics than the shock radius. The energetics of the narrowly collimated jets that drive shock expansion is sensitive to a number of details, e.g., how efficiently energy is extracted from differential rotation, and how much material is entrained by the collimated jets that drive the explosion. It should also be noted that relatively minor differences in the kinetic, magnetic, and thermal energy of the ejecta can translate into larger differences once the potential energy is subtracted. For these reasons, the rather large discrepancy in explosion energy between the AENUS-ALCAR and CoCoNuT-FMT models is not surprising. In Section 4.3, we shall demonstrate that the two codes produce somewhat different PNS structures that can motivate (though not rigorously explain) significant differences in the energetics of the jet-driven explosions.

We will also revisit the sensitivity of the explosion energy in our resolution analysis in Section 5.

The weak-field models appear to be qualitatively more disparate than their strong-field counterparts. All three models have significant delays of  $\sim 400$  ms to the explosion with a slightly longer delay phase for the Alcar-Rw model, mirroring the different time of shock revival (Figure 1). Although the shock radii of all three models are comparable by the end of the simulations, we find pronounced quantitative differences in their explosion energies; the explosion energy of model Alcar-Rw is 80% lower than that of coco-HLLC-Rw, while model coco-HLLE-Rw ends up with a significantly higher explosion energy than the other two models by the end of the simulations. This does not indicate fundamental differences between the codes, but is likely just a reflection of the strongly stochastic explosion dynamics of 2D models in the “hybrid” regime where neutrino heating, convection or SASI, and magnetic fields jointly drive the explosion. The unsteady, and even non-monotonic growth of the explosion energy in coco-HLLC-Rw and Alcar-Rw clearly reveals this stochasticity, and the variations between the different runs are similar to the variations seen in non-magnetic models for different realisations of the same model setup with the same code (Müller 2015; Cardall & Budiardja 2015). This does not, of course, preclude that there are other systematic differences in the dynamics between the weak-field runs that are hidden behind the stochastic variations.

### 4.3 Proto-Neutron Star Parameters and Magnetic Field Amplification

We next consider the bulk parameters and structure of the PNS, and the amplification of magnetic fields inside it as key drivers of the overall dynamics. Figure 4 shows the PNS mass  $M_{\text{PNS}}$ , angular momentum  $J_{\text{PNS}}$ , and magnetic energy  $E_{\text{mag}}$ , which we compute as volume integrals over the region where  $\rho > 10^{11} \text{ g cm}^{-3}$  following the customary, though somewhat arbitrary definition of the PNS surface. The evolution of the angle-averaged PNS radius  $R_{\text{PNS}}$  for the different runs is plotted in Figure 5. Angle-averaged radii are determined by identifying the PNS surface using the same fiducial density  $\rho = 10^{11} \text{ g cm}^{-3}$  based on angle-averaged density profiles.

The growth of the PNS mass (top panel in Figure 4) is very similar in the weak-field models Alcar-Rw, coco-HLLC-Rw and coco-HLLE-Rw runs. We do, however, see an extended period before  $0.35 \text{ s}$  where the CoCoNuT-FMT models have a more massive PNS. The Alcar-Rw model then catches up after  $0.35 \text{ s}$ , and eventually ends up with a slightly more massive PNS. Among the strong-field models, coco-HLLC-Rs and coco-HLLE-Rs exhibit more substantial accretion onto the PNS immediately after collapse compared to model Alcar-Rs, leading to a 9% higher PNS mass in the CoCoNuT-FMT runs throughout. This is explained by the more rapid onset of the explosion seen in Alcar-Rs. The PNS mass difference largely accounts for a similar difference in PNS angular momentum between the CoCoNuT-FMT and ALCAR strong-field models (Figure 4, middle panel).

More dramatic differences between the two codes can be seen in the total PNS angular momenta after about  $0.3 \text{ s}$  post-bounce for the weak-field models. Models coco-HLLC-Rw and coco-HLLE-Rw start to gradually lose angular momentum, whereas model Alcar-Rw continues to slowly gain angular momentum as it accretes mass. This difference is especially noteworthy since the PNS masses of the weak-field models are quite similar throughout. This behaviour in the CoCoNuT-FMT models is likely due to spurious non-conservation of angular momentum due to our numerical implementation in ax-

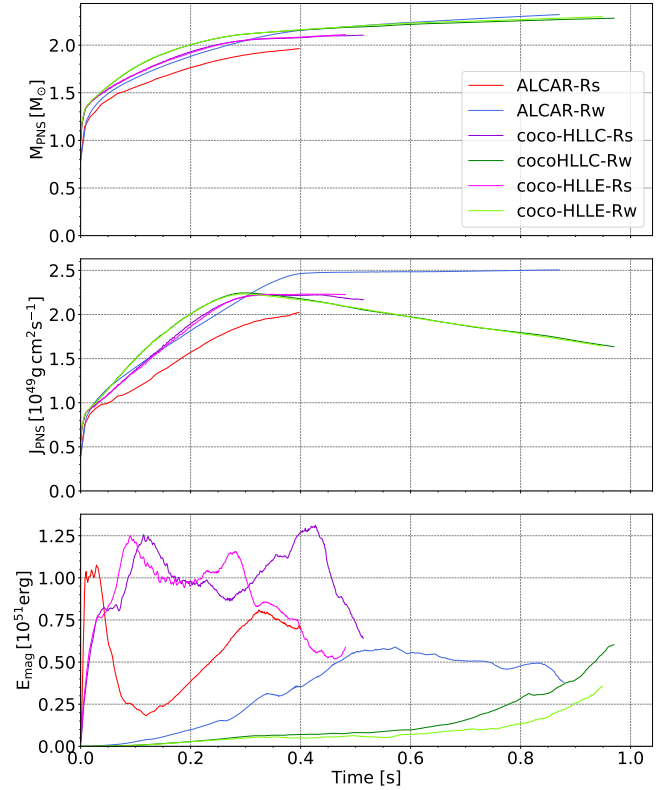


**Figure 4.** PNS mass  $M_{\text{PNS}}$ , angular momentum  $J_{\text{PNS}}$ , and magnetic energy  $E_{\text{mag}}$ , as a function of post-bounce time for the standard-resolution models. The PNS is defined as the region where  $\rho > 10^{11} \text{ g cm}^{-3}$ .

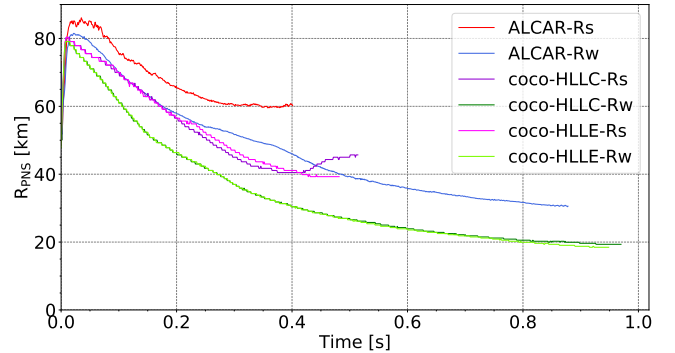


**Figure 5.** Comparison of the time evolution of the angle-averaged PNS radius  $R_{\text{PNS}}$  between the CoCoNuT-FMT and AENUS-ALCAR models.

isymmetry, where the velocity component  $v_\phi$  is zeroed in the zones adjacent to the grid axis. Aside from these boundaries, we shall see that the different treatments of the inner PNS lead to significant differences in the angular momentum profiles between the two codes.

More pronounced differences between the CoCoNuT-FMT and AENUS-ALCAR models than in the PNS mass and angular momentum are found in the PNS magnetic energy  $E_{\text{mag}}$  (bottom panel of Figure 4). In coco-HLLC-Rs and coco-HLLE-Rs, the magnetic energy in the PNS first peaks around  $1.25 \times 10^{51} \text{ erg}$  at  $0.1 \text{ s}$  and remains high for some time, decaying after a second peak. Although the overall time evolution of  $E_{\text{mag}}$  in these two models is quite similar, coco-

HLLC-Rs is set apart by an earlier gradual drop in magnetic energy around 0.1s before coco-HLLC-Rs. This is noteworthy, considering that the choice of Riemann solver shows very little effect on the other PNS quantities. In model Alcar-Rs, the magnetic field energy peaks immediately after core bounce at  $\approx 1.05 \times 10^{51}$  erg, but then decreases sharply to a much lower level.

The weak magnetic field models exhibit similarly large differences as their strong-field counterparts. In particular, we see a much earlier rise in PNS magnetic energy in Alcar-Rw than in coco-HLLC-Rw and coco-HLLC-Rw, followed by a slow, gradual drop after  $\sim 0.5$  s. By contrast, the weak-field runs with CoCoNuT-FMT show a gradual rise in magnetic energy over time that continues until the end of the simulation.

The different evolution of the magnetic field energy results from a combination of effects, as revealed by a closer analysis of radial profiles of the magnetic field energy density. To this end we show spherical averages of the components  $e_{B,r}$ ,  $e_{B,\theta}$ , and  $e_{B,\varphi}$  of the magnetic energy density contained in the radial, meridional, and zonal components of the magnetic field,

$$e_{B,r} = \frac{B_r^2}{8\pi}, \quad e_{B,\theta} = \frac{B_\theta^2}{8\pi}, \quad e_{B,\varphi} = \frac{B_\varphi^2}{8\pi}, \quad (9)$$

for the strong-field case in Figure 6 and for the weak-field case in Figure 7. These profiles of the magnetic energy are best viewed in conjunction with angle-averaged profiles of the specific angular momentum, which is computed as

$$j = \frac{\int \rho v_\varphi r \sin \theta d\Omega}{\int \rho d\Omega}. \quad (10)$$

Profiles of  $j$  at different times are presented in Figure 8 and Figure 9 for the strong- and weak-field case, respectively.

Both for the weak- and strong-field case, the profiles of  $e_{B,r}$ ,  $e_{B,\theta}$ , and  $e_{B,\varphi}$  are very similar at bounce, i.e., field amplification during the collapse phase in the inner core is consistent between the two codes despite the different treatment of the induction equation. Later, however, the situation changes for two reasons.

In the strong-field case, we first see a steady drop of magnetic field energy in the innermost few kilometres in the ALCAR-Rs run because the inner core is treated in low-resolution 2D, leading to more numerical diffusion. In model coco-HLLC-Rs, strong field dissipation in the core is avoided by enforcing uniform rotation and spherical symmetry in the meridional flow components in the innermost 10 km. Second, we see stronger field amplification in model coco-HLLC-Rs around a radius of 20 km, primarily in  $e_{B,\varphi}$  and to a lesser extent in  $e_{B,r}$ , which is indicative of strong shear amplification at the PNS surface. This is consistent with the finding that the angular momentum profiles show a hump around 20 km in model coco-HLLC-Rs, whereas the specific angular momentum plateaus outside the PNS than in Alcar-Rs (Figure 8). This implies a steeper negative angular velocity gradient, i.e., stronger shear, in around and outside 20 km in coco-HLLC-Rs. The stronger fields generated around these radii in coco-HLLC-Rs also translate into stronger fields in the jet in the long term; the components  $e_{B,r}$  and  $e_{B,\varphi}$  are about a factor ten higher at the maximum shock radius at late times. The profiles of  $e_{B,r}$  reveal a numerical disadvantage of the divergence cleaning scheme as originally implemented in CoCoNuT-FMT; choosing the maximum cleaning speed allowed by the CFL limit results in spurious transport of magnetic energy into the pre-shock region. The different treatment of the inner core in both codes has further implications for the long-term evolution of magnetic fields in the PNS. While Alcar-Rs initially loses magnetic field energy in the innermost zones, it also shows stronger field amplification in  $e_{B,\theta}$  just inside 10 km in

contrast to CoCoNuT-HLLC-Rs. This is due to the inclusion of differential rotation of the inner core in the Alcar code, which allows for field amplification in this region that is responsible for the rise in the PNS magnetic energy  $E_{\text{mag}}$  after the very rapid decreases in magnetic energy in  $e_{B,r}$ ,  $e_{B,\theta}$ , and  $e_{B,\varphi}$  from numerical dissipation in the innermost zones (cp. Figure 4).

The different evolution of the PNS magnetic energy in the weak-field case (with a faster rise in AENUS-ALCAR than in CoCoNuT-FMT) can also be understood as a consequence of the different core treatment. Model Alcar-Rw again shows field amplification by differential rotation inside the core whereas CoCoNuT-HLLC-Rw only shows a slow decline in  $e_{B,r}$  and  $e_{B,\theta}$  and a slow rise in  $e_{B,\varphi}$  by compression inside the innermost 10 km. Interestingly, the (putatively numerical) decline of the magnetic field energy in the innermost zones is less pronounced in model Alcar-Rw than in model Alcar-Rs, suggesting that this phenomenon is very sensitive to the dynamics near the origin of the grid. Field amplification in the differentially rotating PNS core generates substantial toroidal fields, which dominate the PNS magnetic energy; ultimately, the toroidal component of the magnetic energy density is increased relatively uniformly out to a radius of about 20–30 km. By contrast, field amplification in model coco-HLLC-Rw is confined to the PNS surface region outside the uniformly rotating core at radii of 10–20 km. Similar to the strong-field case, the amplification of the toroidal field by shear in this region is stronger than in the ALCAR model. Due to the stronger field amplification at the PNS surface, the PNS magnetic energy in model CoCoNuT-HLLC-Rw eventually overtakes model Alcar-Rw at late times, overcompensating for the spurious lack of field amplification inside the PNS.

The angular momentum profiles of models coco-HLLC-Rs and Alcar-Rs (Figure 8) and of models coco-HLLC-Rs and Alcar-Rs (Figure 9) yield more insights into the causes of the different patterns of field amplification in the CoCoNuT and ALCAR models. The strong-field model coco-HLLC-Rs shows the build-up of a hump in specific angular momentum outside the PNS centred at radii of 40–50 km in the late-time profiles. The presence of such a hump implies considerable shear in and above the PNS surface region, which explains the strong magnetic fields generated in this layer in model coco-HLLC-Rs (Figure 6). In model Alcar-Rs, the hump is less pronounced, more smeared out, and located further outside. In the early profiles, where the hump is yet absent, the transition to a plateau in specific angular still occurs further outside in model Alcar-Rs compared to coco-HLLC-Rs, implying less shear and less field amplification in the PNS surface region. Further analysis reveals that the different angular momentum distribution in the two runs is related to the different PNS radii seen in Figure 5; effectively the PNS has more fluffy, disk-like surface in model Alcar-Rs. It is difficult to decide a priori which of the codes captures the structure of the disk-like surface region more accurately. We shall see in Section 5 that CoCoNuT-FMT also tends to produce more a more fluffy PNS surface at higher resolution. This tentatively suggests that the more fluffy PNS surface structure with a flatter angular momentum distribution is more realistic.

The angular momentum profiles deeper in the PNS also reveal an interesting phenomenon. In model Alcar-Rs, there is a clear secular drop in angular momentum at radii of less than 10 km, whereas model coco-HLLC-Rs shows little changes in the angular momentum profiles in this region. One might be tempted to connect the slow-down of PNS rotation with numerical diffusion of angular momentum into the innermost zone, where the angular momentum drops dramatically. However, the fact that the secular slow-down of PNS rotation is much less pronounced in model Alcar-Rw (Figure 9) suggests that numer-

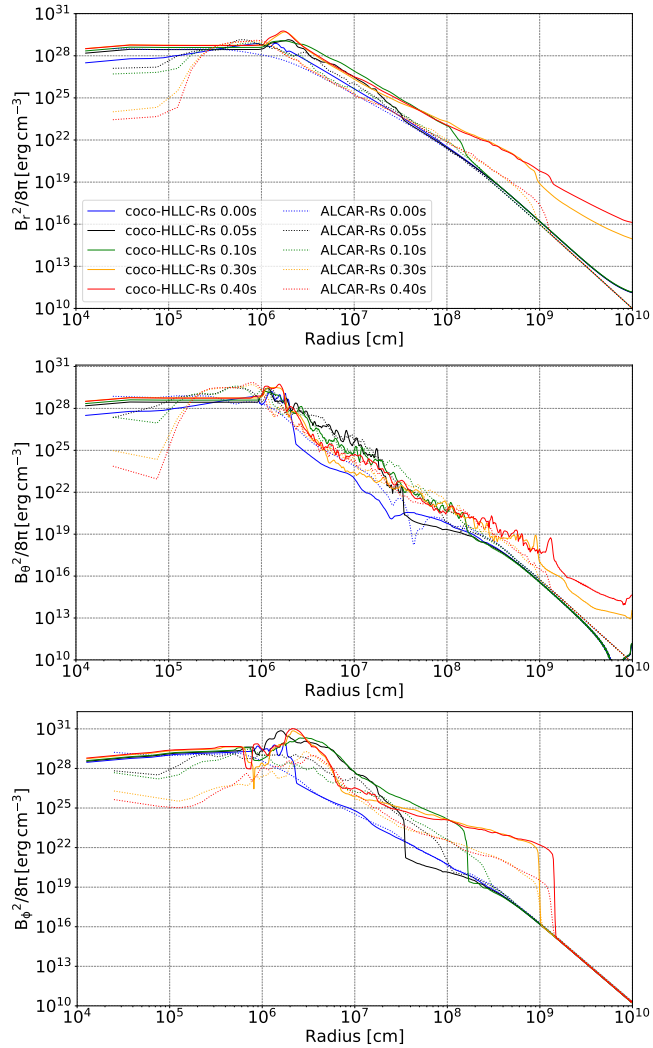


**Figure 6.** Top to bottom: Profiles of the energy density contained in the radial, meridional, and zonal components  $B_r$ ,  $B_\theta$ , and  $B_\phi$  of the magnetic field for the strong-field models coco-HLLC-Rs (solid lines) and Alcar-Rs (dashed lines) at various post-bounce times.

ical diffusion of angular momentum only plays a secondary role. Instead, the slow-down of core rotation in model Alcar-Rs appears to be connected to the action of magnetic stresses that initially build up due to field winding and then become strong enough to make the inner core spin more slowly (akin to the winding and unwinding of a spring). This is reflected by the decreasing toroidal field strength in the innermost zones in model Alcar-Rs at late times (Figure 6, bottom panel), and the process of winding and unwinding also contributes to the long-period oscillation in the PNS magnetic energy in this model (Figure 4, bottom panel). In the angular momentum profile at 0.05 s, we find an interesting trace of such long-term torsional motions in the form of a dip in the specific angular momentum outside a radius of 10 km (Figure 8). The long-period oscillations due to the winding and unwinding of the field are absent in the CoCoNuT-FMT models because the inner core is forced to rotate uniformly.

The angular momentum profiles of the weak-field models Alcar-Rw and coco-HLLC-Rw are much more similar (Figure 9). Both models develop humps in their angular momentum profiles with sharp angular momentum gradients at the outer flank of the hump.

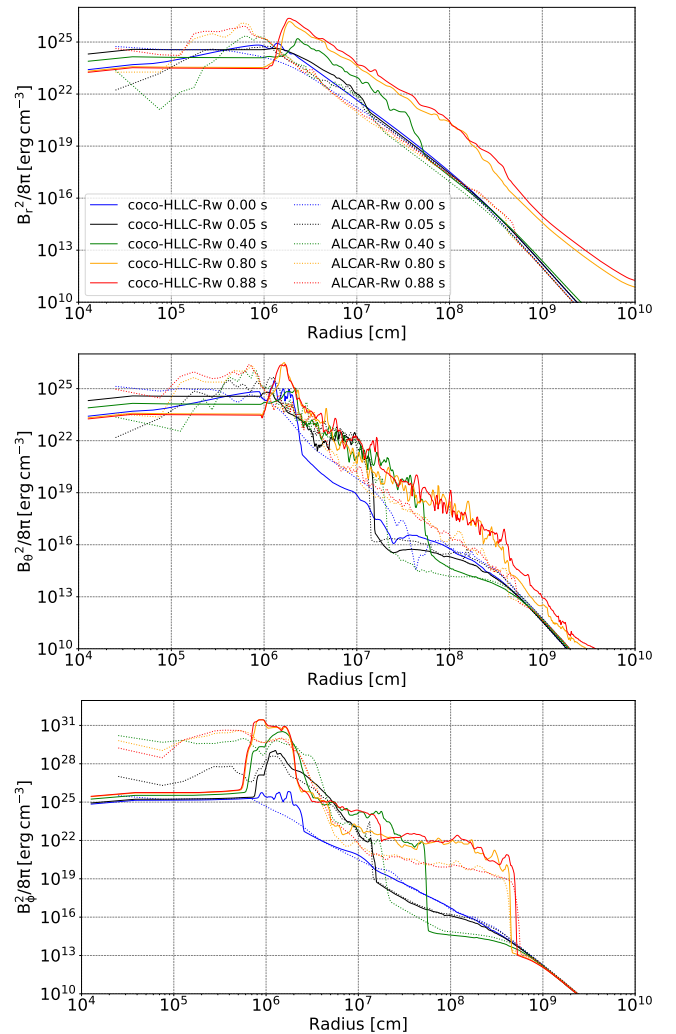


**Figure 7.** Top to bottom: Profiles of the energy density contained in the radial, meridional, and zonal components  $B_r$ ,  $B_\theta$ , and  $B_\phi$  of the magnetic field for the weak-field models coco-HLLC-Rw (solid lines) and Alcar-Rw (dashed lines) at various post-bounce times.

The humps are, however, located at different radii, which reflects the aforementioned tendency towards a more inflated PNS surface structure in Alcar (cp. Figure 5). The evolution of the angular momentum profile in the PNS core is quite similar despite different numerical treatments for this region. Different from the strong-field model, magnetic stresses remain too weak to substantially affect the rotational evolution of the PNS core over the time scales of the simulation. Model coco-HLLC-Rw has higher specific angular momentum at radii less than about 3 km, possibly avoiding a slight loss of angular momentum into the central zone in Alcar-Rw. On the other hand, it does not capture the moderate amount of differential rotation in the PNS core due to its core treatment, while Alcar-Rw maintains the profile of differential rotation quite stably after an initial drop of specific angular momentum in the innermost zones in the first 50 ms after bounce.



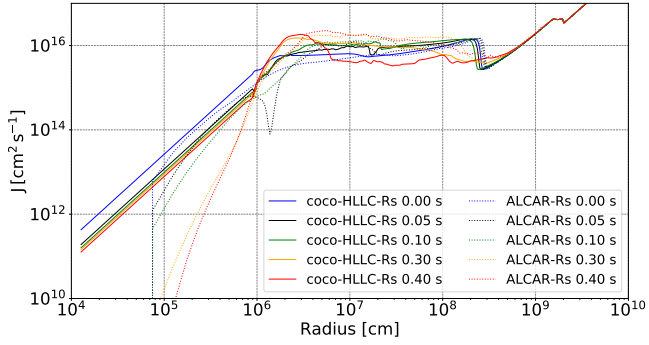


**Figure 8.** Spherically averaged specific angular momentum as a function of radius at different post-bounce times for the strong-field models Alcar-Rs (dotted lines) and coco-HLLC-Rs (solid lines).

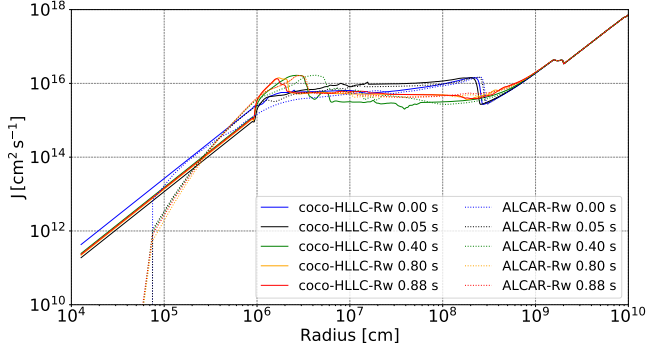


**Figure 9.** Spherically averaged specific angular momentum as a function of radius at different post-bounce times for the weak-field models Alcar-Rw (dotted lines) and coco-HLLC-Rw (solid lines).

#### 4.4 Neutrino Emission

Even in a magnetorotational supernova, neutrinos still play a major role by influencing the nucleosynthesis conditions in the outflows (e.g., Janka 2012), and in some cases also by providing subsidiary energy input into the outflows. Since the fast-multi group transport scheme used in CoCoNuT-FMT (Müller & Janka 2015) and the two-moment method implemented in AENUS-ALCAR (Just et al. 2015) represent quite different approaches to multi-group neutrino transport, and since the codes do not use exactly the same set of neutrino interaction rates, differences in the neutrino emission between the two codes are expected. However, the impact of the transport treatment on the neutrino emission can hardly be disentangled from the effect of the PNS structure, which is sensitive to the multi-dimensional dynamics of the models as outlined in the previous section. In contrast to 1D code comparisons, it would be a futile undertaking to fully track down the cause for all the differences in the neutrino emission. We therefore compare the neutrino emission in the two codes at a rather descriptive level, only occasionally highlighting phenomena that can be traced either to differences in the neutrino transport or to the model dynamics with greater confidence.

Neutrino luminosities for the various ALCAR models and the standard-resolution CoCoNuT model are shown in Figure 10 and reveal substantial differences. Neutrino mean energies are shown in Figure 11.

Especially at early times, the neutrino luminosities of all flavours tend to be higher in the CoCoNuT models, while the corresponding

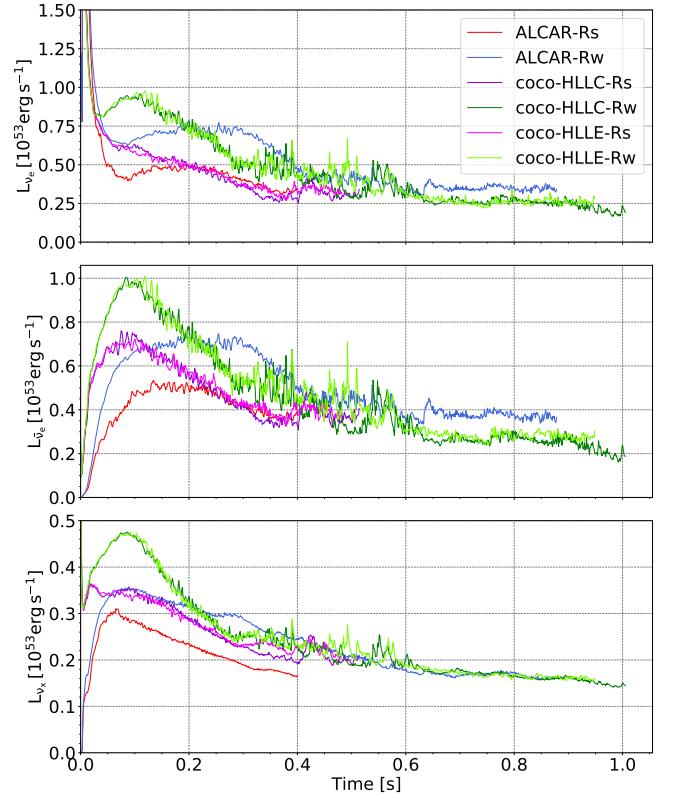


**Figure 10.** Neutrino luminosities of electron neutrinos ( $\nu_e$ , top row), electron antineutrinos ( $\bar{\nu}_e$ , middle) and heavy-flavour neutrinos ( $\nu_x$ , bottom), measured at a radius of 2000 km.

CoCoNuT models with the HLLC and HLLE solver show very similar luminosities. The higher early luminosities in CoCoNuT reflect differences in the collapse dynamics and early post-bounce accretion rate (Figure 2) that were discussed in Section 4.1.

The temporal evolution of the neutrino mean energies is qualitatively similar, but CoCoNuT models are characterised by somewhat higher mean energies throughout, except for the heavy-flavour neutrinos.

In the case of the strong-field models, the electron neutrino and antineutrino luminosity is higher by up to  $2 \times 10^{52} \text{ erg s}^{-1}$  in models coco-HLLC-Rs and coco-HLLE-Rs compared to Alcar-Rs during the first  $\sim 100$  ms after bounce and then gradually become more similar to the ALCAR model. The higher electron-flavour mean energies are consistent with smaller PNS radii in CoCoNuT; the combination of smaller radii and higher surface temperatures fortuitously leads to similar neutrino luminosity as in ALCAR after  $\sim 200$  ms. Note that unlike the electron-flavour luminosity, which is affected by differences in the early post-bounce accretion rate, the heavy-flavour luminosity remains consistently higher in the strong-field CoCoNuT models throughout the simulation. The faster contraction of the PNS in CoCoNuT alone cannot account for the stronger emission since the heavy-flavour neutrino mean energy is not substantially higher in CoCoNuT. Different interaction rates likely play a substantial role here. The omission of electron-positron annihilation in CoCoNuT can theoretically push the luminosity and mean energy up or down depending on the gradient of the temperature and chemical potentials near the neutrinosphere, the effective treatment of neutrino-nucleon scattering will tend to push the neutrino luminosity and mean energy

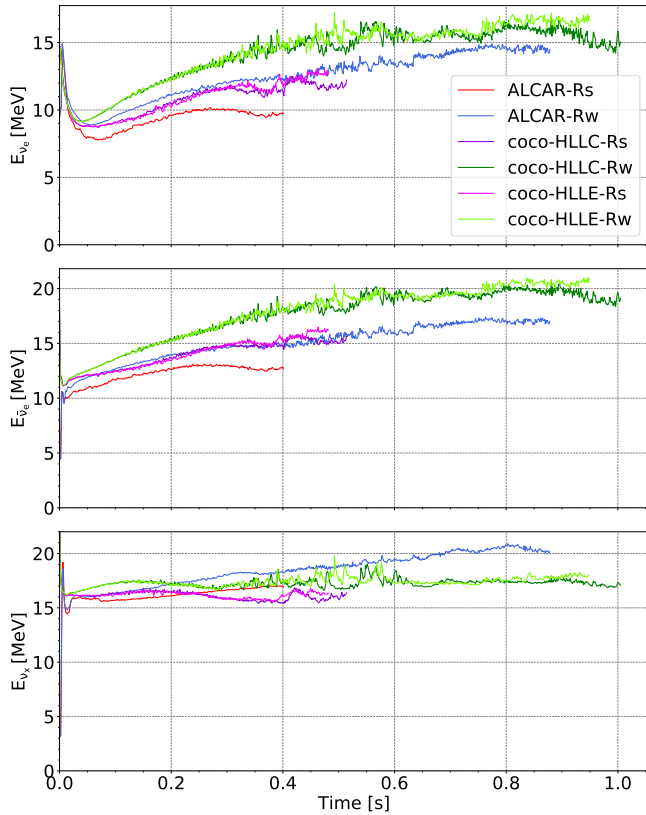


**Figure 11.** Neutrino mean energies of electron neutrinos ( $\nu_e$ , top), electron antineutrinos ( $\bar{\nu}_e$ , middle) and heavy-flavour neutrinos ( $\nu_\chi$ , bottom), measured at a radius of 2000 km.

down, and the strangeness corrections and nucleon correlations will likely push them upwards.

It is noteworthy that there is a marked divergence between models coco-HLLC-Rs and coco-HLLE-Rs after  $\sim 0.4$  s, which is when coco-HLLC-Rs develops a more fluffy PNS surface structure than coco-HLLE-Rs (Figure 4). At this point, the electron-flavour mean energies in model coco-HLLC-Rs drop below those in coco-HLLE-Rs by about 1 MeV. Model coco-HLLC-Rs also exhibits a noticeably smaller heavy-flavour luminosity than coco-HLLE-Rs from 0.3 s onward. While the variations between these two models are considerably smaller than the differences between the CoCoNuT and ALCAR models, this illustrates that neutrino luminosities and mean energies show considerable sensitivity to subtle dynamical variations in multidimensional MHD supernova models of rapidly rotating progenitors.

Among the weak-field models, we see similar differences in the early neutrino emission that can be ascribed to the same effects as for the strong-field models. In contrast to the strong-field models, there is, however, a cross-over in the electron flavour luminosities, with a phase of higher luminosities in Alcar-Rw compared to coco-HLLC-Rw and coco-HLLE-Rw. This is again consistent with the mass accretion rates in the two codes. At late times, the CoCoNuT models again exhibit higher electron-flavour luminosities; at this junction the more compact PNS surface structure is likely part of the explanation. Interestingly, the heavy-flavour luminosities and mean energies become similar between ALCAR and CoCoNuT at late times. As heavy-flavour neutrinos originate from higher densities, these are less affected by the different “fluffiness” of the PNS surface structure in the two codes.

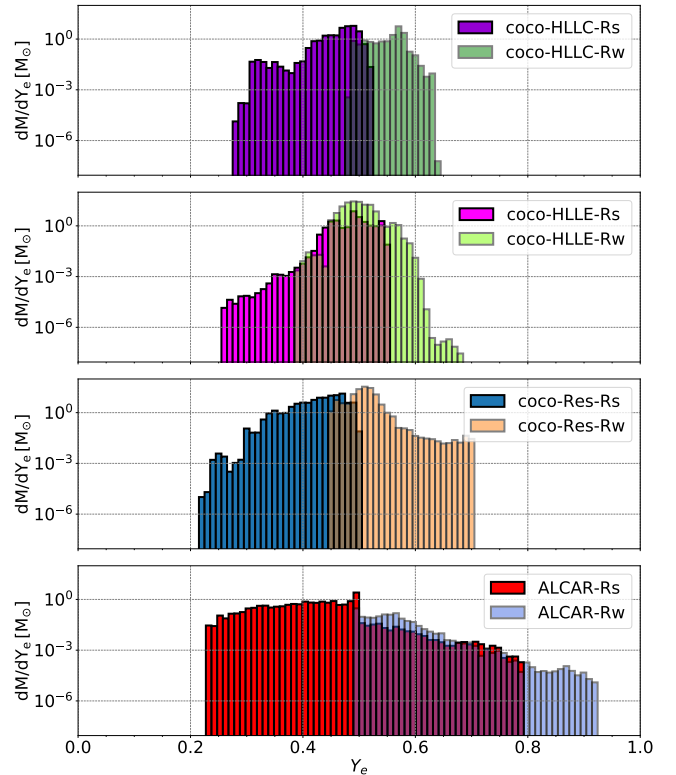


**Figure 12.** Histograms of the electron fraction  $Y_e$  of the ejecta for the strong-field models at  $\approx 0.40$  s and at  $\approx 0.85$  s for the weak-field models. The four panels show, from top to bottom, the  $Y_e$ -distribution in the coco-HLLC, coco-HLLE, coco-Res and Alcar models, respectively.

The above results suggest that agreement between different codes in the neutrino luminosities and mean energies can only be achieved at a level of 10–20% in MHD models of rapidly rotating supernova progenitors. This is decidedly worse than what was achieved in the comparison between the FMT transport scheme and the VERTEX neutrino transport code in Müller & Janka (2015) in the non-rotating case. The interplay between the multidimensional dynamics and the neutrino emission proves a considerable obstacle in analysing and eliminating code-dependent differences in the neutrino emission.

#### 4.5 Nucleosynthesis Conditions

Because of the ejection of neutron-rich material of relatively high entropy in the MHD-powered jets, magnetorotational supernovae have been proposed as an alternative site for the rapid neutron capture process (r-process, e.g., Winteler et al. 2012; Hafevi & Mösta 2018; Grimmert et al. 2021; Reichert et al. 2021). This is supported by observational indications for r-process enrichment in low-metallicity environments that may be difficult to explain by neutron stars mergers (Nishimura et al. 2015; Kobayashi et al. 2020). In this context, it is important to analyse whether the different neutrino emission in ALCAR and CoCoNuT has a substantial impact on the nucleosynthesis conditions in the outflows.

To this end, we visualise the distribution of the electron fraction  $Y_e$  in the ejecta in the different models using histograms for all the weak- and strong-field models (Figure 12). The unbound ejecta are taken to comprise material with positive total specific energy, positive radial velocity, and a density lower than  $10^{11} \text{ g cm}^{-3}$  in order not to

accidentally include material in the PNS. Histograms are plotted at a post-bounce time of  $\approx 0.4$  s for coco-HLLC-Rs, coco-HLLE-Rs, and Alcar-Rs, and at  $\approx 0.85$  s for coco-HLLC-Rw, coco-HLLE-Rw, and Alcar-Rw.

All the strong-field models show a neutron-rich tail in the ejecta distribution that extends down to values of  $Y_e$  as low as 0.25–0.3, as well as a smaller amount of proton-rich ejecta. Neutron-rich conditions arise in matter that is quickly ejected in the magnetically collimated jets from close to the PNS so that  $Y_e$  freezes out at low values before it can be raised by neutrino irradiation (Wanajo et al. 2011; Müller 2016). In slowly moving ejecta, neutrino absorption tends to establish proton-rich conditions because of similar  $\nu_e$  and  $\bar{\nu}_e$  luminosities and small differences between the  $\nu_e$  and  $\bar{\nu}_e$  mean energies (Fröhlich et al. 2006; Pruet et al. 2006). In all the weak-field models, which do not develop fast jets, the ejecta are predominantly proton-rich, similar to recent multi-D models of neutrino-driven explosion using multi-group neutrino transport (Wanajo et al. 2018; Eichler et al. 2018; Burrows et al. 2020), although all models contain small amounts of neutron-rich ejecta except for Alcar-Rw.

Despite the differences in the neutrino-emission between CoCoNuT and ALCAR, the qualitative shape of the  $Y_e$ -distribution is quite similar in all models. This is not as surprising as it might first seem, since  $Y_e$  is less sensitive to the absolute values of the neutrino luminosities and mean energies than to the differences between electron neutrinos and antineutrinos, which are similar for both codes.

Nonetheless, we still find noticeable quantitative differences in the  $Y_e$ -distribution. Once more, disentangling how the numerical methods and approximations employed in the two codes shape the distribution proves difficult, but a few plausible effects can be discerned.

Among the strong-field models, coco-HLLE-Rs has the least amount of material with  $Y_e < 0.4$ . This is consistent with the more diffusive nature of the HLLE solver, which will tend to raise  $Y_e$  in the jets by numerical mixing with less neutron-rich material. However, the lowest  $Y_e$  in model coco-HLLE-Rs is even *lower* than in coco-HLLC-Rs, even though the total amount of material below  $Y_e < 0.4$  is substantially smaller. This is not a contradiction because the HLLE solver sometimes produces more violent, unsteady flow with bigger flow structures in the subsonic regime (Müller 2009). The amount of strongly neutron-rich material in Alcar-Rs is higher than in the CoCoNuT models and  $Y_e$  reaches lower minimum values (0.23 in Alcar-Rs as opposed to 0.28 in coco-HLLC-Rs). However, it is not possible to disentangle whether this is due to less severe numerical dissipation, different jet dynamics, or the neutrino transport treatment. The neutrino transport likely plays some role because model Alcar-Rs shows a rather remarkable proton-rich tail up to  $Y_e = 0.8$ , whereas the strong-field CoCoNuT models only eject moderately proton-rich material. It is unlikely that numerical diffusion alone could compress the distribution of proton-rich material so significantly as to explain the narrow distribution in the CoCoNuT model on its own.

The  $Y_e$ -distributions in the weak-field models agree inasmuch as the bulk of the ejecta fall into the moderately proton-rich range of  $Y_e = 0.5$ –0.6. However, one notices a more extended proton-rich tail in Alcar-Rw compared to the CoCoNuT-FMT models. Unlike model Alcar-Rw, the CoCoNuT models also have a small admixture of slightly neutron-rich ejecta. Interestingly, the  $Y_e$ -distribution in model coco-HLLE-Rw is broader than in coco-HLLC-Rw and shifted to slightly smaller values. From the viewpoint of nucleosynthesis, the impact of the Riemann solver appears quite substantial. A shift of the minimum  $Y_e$  from 0.48 in coco-HLLC-Rw to about 0.39 in coco-HLLE-Rw will imply a considerable change in iron-group

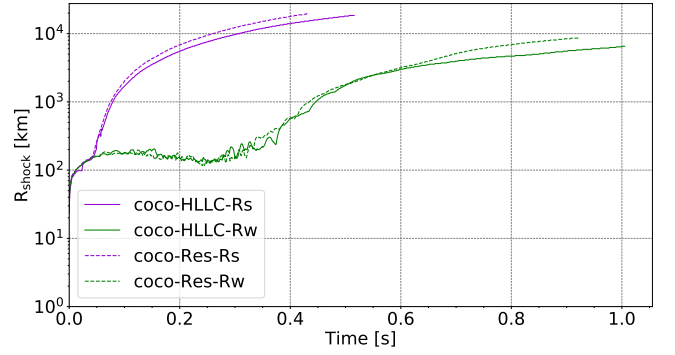


**Figure 13.** Evolution of the maximum shock radius for the coco-HLLC models at standard resolution compared to the corresponding high-resolution coco-Res models. Both the weak- and strong-field case are shown. The radius given in a log<sub>10</sub> scale.

nucleosynthesis from NSE freeze-out from a predominant contribution of  $^{56}\text{Ni}$  to a substantial contribution of neutron-rich nuclides like  $^{60}\text{Fe}$  and  $^{48}\text{Ca}$  (Wanajo et al. 2018; Hartmann et al. 1985) and others. In summary, our code comparison so far already suggests that yields from the tail of the  $Y_e$ -distribution in MHD supernova models are expected to be quite sensitive to numerical details, whereas the composition of the bulk of the ejecta close to  $Y_e = 0.5$  appears more robust. This suggests that the models can be more confidently used to predict  $^{56}\text{Ni}$  yields that are relevant for supernova light curves, as  $^{56}\text{Ni}$  is produced in the regime close to and above  $Y_e = 0.5$ , whereas r-process yields from simulations may be prone to considerable uncertainties.

## 5 RESULTS – RESOLUTION STUDY

To supplement the code comparison in Section 3, we compare models coco-HLLC-Rs and coco-HLLC-Rw to the corresponding high-resolution models coco-Res-Rs and coco-Res-Rw, which have been calculated with an angular resolution of  $0.7^\circ$  (256 zones) instead of  $1.4^\circ$  (128 zones). By revisiting parts of the analysis in Section 4 we shall not only explore a further dimension of uncertainties in MHD supernova models, but also obtain clues about the reasons underlying the differences between ALCAR and CoCoNuT models.

### 5.1 Shock Propagation and Explosion Energy

Figures 13 and 14 show the shock trajectories and explosion energies of the standard- and high-resolution models as the simplest global metrics of the dynamics. Among the strong-field models, we note that the high-resolution model coco-Res-Rs exhibits somewhat faster shock expansion than the baseline model coco-HLLC-Rs. The explosion energy is lower in coco-Res-Rs, however, and grows only at a rate of  $\approx 1.7 \times 10^{51} \text{ erg s}^{-1}$  as opposed to  $\approx 2 \times 10^{51} \text{ erg s}^{-1}$  in coco-HLLC-Rs. This suggests that uncertainties of order  $\sim 10\%$  in these global quantities are expected due to limitations in resolution, or possibly from stochastic model variations (cp. Cardall & Budiardja 2015) alone. We note that the small explosion energy of the high-resolution model is not at odds with the resolution study of Sawai & Yamada (2016), who found a faster growth of the explosion energy for higher resolution in MHD-driven supernova models, but considered a somewhat different scenario. Sawai & Yamada (2016) started their simulations with smaller seed fields and attempted to

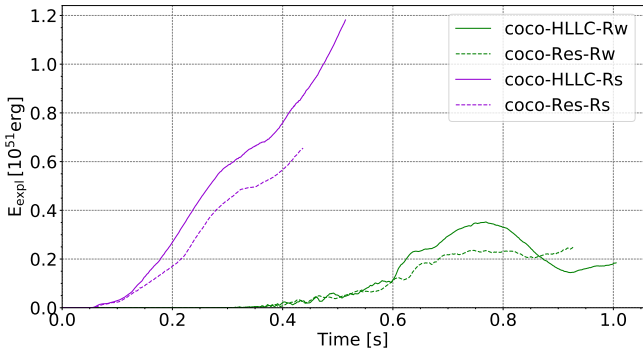


**Figure 14.** Comparison of the evolution of the diagnostic explosion energy  $E_{\text{expl}}$  in the strong- and weak-field models coco-HLLC at standard resolution to the corresponding high-resolution coco-Res models.

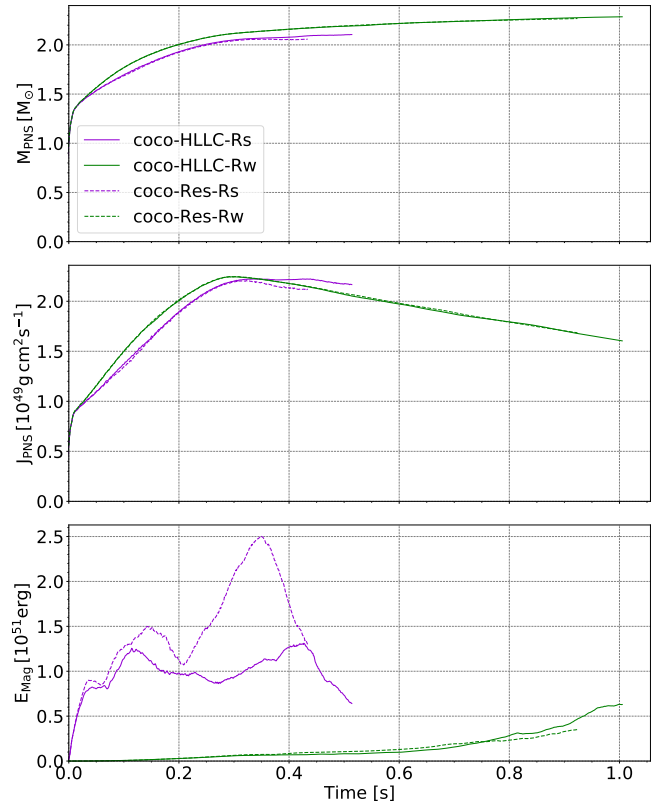
follow field amplification by the MRI using very high resolution *inside* the PNS, whereas our simulations start with sufficiently strong fields to promptly trigger a magnetorotational explosion.

For the weak-field models, we observe small differences in the shock propagation and explosion energy between models coco-Res-Rw and coco-HLLC-Rw as well. Towards the end of the simulations, coco-Res-Rw has a larger maximum shock radius, but the difference in shock propagation is quite variable over time. Similarly, coco-Res-Rw has a lower explosion energy until 0.9 s but then overtakes model coco-HLLC-Rw. The variations between these two models may thus be purely stochastic in nature.

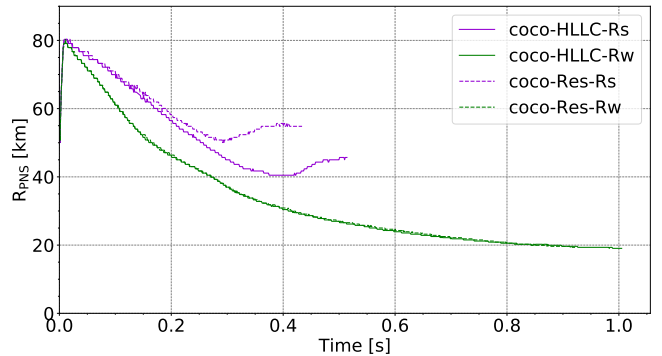
## 5.2 Proto-neutron Star Structure and Neutrino Emission

Figure 15 shows the PNS mass, angular momentum, and magnetic energy for models coco-Res-Rs, coco-Res-Rw, coco-HLLC-Rs, and coco-HLLC-Rw. In the weak-field case, the high-resolution and standard-resolution runs show almost perfect agreement in these quantities. There is only a hint of a slightly faster rise of the PNS magnetic energy in coco-HLLC-Rw close to the end of the simulation. However, more substantial differences emerge between the strong-field models coco-HLLC-Rs and coco-Res-Rs. After about 0.3 s, the PNS angular momentum in model coco-Res-Rs starts to decrease faster than in coco-HLLC-Rs and ends up with a 5% smaller value. More intriguingly, the PNS magnetic energy in model coco-Res-Rs peaks at almost double the value in coco-HLLC-Rs. The evolution of the PNS radius also differs significantly (Figure 16). Model coco-Res-Rs shows significant radius inflation at about 0.3 s, and while a similar phenomenon occurs in the standard-resolution run, this happens about 0.1 s later. This is noteworthy because a similar divergence of the PNS radii was found in our comparison between the strong-field ALCAR and CoCoNuT models in Section 4. This is a further indication that the PNS surface region is subject to some form of tipping process that results in the adjustment to a more stable structure under conditions that are highly sensitive to the numerical implementation and grid resolution. Models coco-HLLC-Rs and coco-Res-Rs offer an opportunity to visualise the compact and inflated state of the PNS more clearly.

In Figure 18 (left panel), we show 2D plots of the entropy in the innermost 100 km of the grid in models coco-Res-Rs and coco-HLLC-Rs. In both cases, the PNS has a strongly oblate structure, and its surface even forms something of a torus or thick disk. In the high-resolution model coco-Res-Rs, the disk-like structure is considerably more extended than in model coco-HLLC-Rs. We note



**Figure 15.** Comparison of the PNS mass  $M_{\text{PNS}}$ , angular momentum  $J_{\text{PNS}}$ , and magnetic energy  $E_{\text{mag}}$ , as a function of post-bounce time for the standard-resolution coco-HLLC models and the high-resolution coco-Res models. The PNS is defined as the region where  $\rho > 10^{11} \text{ g cm}^{-3}$ .



**Figure 16.** Comparison of the time evolution of the angle-averaged PNS radius  $R_{\text{PNS}}$  between CoCoNuT-FMT models with different resolution.

that the edge of the PNS accretion disk at about 50 km in coco-HLLC-Rs corresponds to the steep gradient in angular momentum profile at late times in this model (Figure 17, cp. also Figure 8). This suggests that the inflation of the disk is caused by outward angular momentum transport from the inner regions of the PNS by strong magnetic fields to larger radii. This is consistent with our interpretation that the different angular momentum profiles in the ALCAR and CoCoNuT discussed in Section 4 are due a bifurcation instability that leads to a different PNS surface structure when triggered.

We can see a similar effect, albeit at smaller level, in the compar-



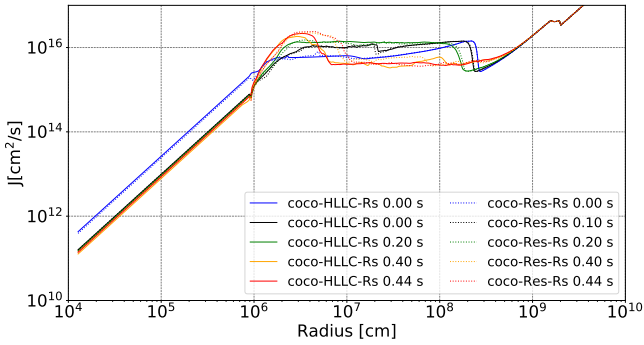


**Figure 17.** Spherically averaged specific angular momentum as a function of radius at different post-bounce times for the strong-field models coco-Res-Rs (dotted lines) and coco-HLLC-Rs (solid lines).

ison between models coco-HLLE-Rs and coco-HLLC-Rs with the latter exhibiting a more fluffy disk structure than the HLLE model (Figure 18, right panel). Intriguingly, the more dissipative Riemann solver produces a disk structure that is less inflated than with the more accurate HLLC solver. Less numerical dissipation on the grid scale – either due to the use of a more accurate solver or higher resolution – seems to enhance rather than to inhibit angular momentum transport. This appears counterintuitive at first glance, but there are other known instances of instabilities being *suppressed* by insufficient numerical dissipation, e.g., spurious behaviour of the Kelvin-Helmholtz instability in smoothed-particle hydrodynamics can be cured by introducing appropriate artificial conductivity at contact discontinuities (Price 2008). On the other hand, the instability could still arise more easily at higher resolution due to increased small-scale numerical noise. Alternatively, the instability might be triggered by stronger magnetic field amplification in model coco-Res-Rs (Figure 15, bottom panel).

Regardless of the reason, the divergent disk structures in models coco-HLLC-Rs, coco-Res-Rs, and coco-HLLE-Rs further illustrate that the dynamics of MHD supernova models is highly sensitive to details of the numerical implementation such as the Riemann solver, and to the grid resolution, even though some bulk metrics like the explosion energy do not immediately show the same strong dependency.

Unsurprisingly, the variations in PNS surface structure among the strong-field CoCoNuT models are also reflected in the neutrino emission. Neutrino luminosities and mean energies for all neutrino species for the weak- and strong-field HLLC models at different resolution are shown in Figures 19 and 20, respectively. The neutrino luminosities hardly show any resolution dependence, and neither do the mean energies for the weak-field models. However, the onset of disk inflation in model coco-Res-Rs translates into a marked divergence of the neutrino energies of all flavours from model coco-HLLC-Rs. At the end of the simulation, the mean energies of the electron flavour neutrinos are about 2 MeV lower, which is comparable to the differences between ALCAR and CoCoNuT, and consistent with the significant expansion of the PNS radius in coco-Res-Rs.

### 5.3 Nucleosynthesis Conditions

Finally, we show histograms of the  $Y_e$ -distribution of the ejecta in model coco-Res-Rs and coco-Res-Rw in Figure 12. As in Section 4.5, the distribution is computed for the unbound outflowing material at

$\approx 0.40$  s for the strong-field case and at  $\approx 0.85$  s for the weak-field case.

We notice much more extended tails in the high-resolution models. In model coco-Res-Rs, the neutron-rich tail reaches down about as far as in the ALCAR model to 0.21, even though the amount of very neutron-rich material is still smaller than in ALCAR. In model coco-Res-Rw, the proton-rich tail is now also quite flat as in model Alcar-Rw, only that a numerical cut-off is applied at  $Y_e = 0.7$ , corresponding to the upper boundary of the low-density NSE table that is used above temperatures of 4.5 GK. However, the ejecta in model coco-Res-Rw still cluster more strongly at a slightly proton-rich value of 0.7 than in Alcar-Rw.

It is noteworthy that the impact of the grid resolution and the Riemann solver on the  $Y_e$ -distribution is of a similar magnitude as the differences between the CoCoNuT and ALCAR models, i.e., between codes with independent and rather dissimilar neutrino transport schemes. While the impact on actual yields would have to be evaluated by detailed post-processing of the nucleosynthesis, the sensitivity of the  $Y_e$ -distribution suggests that r-process yields from current magnetorotational supernova models may still be subject to substantial quantitative uncertainties as these hinge on the neutron-rich tail of the ejecta distribution.

## 6 CONCLUSIONS

We conducted the first code comparison of 2D MHD supernova models with the two independent codes CoCoNuT-FMT and AENUS-ALCAR. Starting from the same initial conditions, we simulated the collapse and explosion of a rapidly rotating helium star progenitor model with an initial helium star mass of  $35M_\odot$  (Woosley & Heger 2006) for two initial magnetic field configurations with the same dipole geometry but different initial field strengths. The initial poloidal and toroidal field strengths are chosen as  $B_{\text{pol,tor}} = 10^{12}\text{G}$  in the strong-field case and as  $B_{\text{pol,tor}} = 10^{10}\text{G}$  in the weak-field case. For the CoCoNuT-FMT code, we also investigated the impact of different Riemann solvers (HLLC and HLLE) and the grid resolution CoCoNuT-FMT in a minimal resolution study.

We find overall qualitative agreement between the codes. Both in the strong-field case and in the weak-field case CoCoNuT and ALCAR yield explosions at similar times with broadly similar shock trajectories. Nonetheless, quantitative differences emerge upon closer inspection. Even within the same code, there is an appreciable sensitivity to numerical details like the Riemann solver and the grid resolution, although the various CoCoNuT models are still more similar to each other than to the corresponding ALCAR run.

Notable differences include a more rapid explosion in the strong-field ALCAR model compared to CoCoNuT-FMT, which translates into a significantly higher explosion energy. At the end of the simulations, the explosion energies still differ by tens of percent, even though the relative difference may shrink on longer time scales. Similarly, large differences in explosion energy are found for the weak-field models, although these may be impacted by stochastic model variations. Closer inspection reveals differences that can be traced to, or plausibly be associated with the disparate numerical schemes used in the two codes. The treatment of the innermost 10 km in CoCoNuT-FMT as a quasi-spherical, uniformly rotating region leads to systematic differences in field amplification in the PNS. The two codes also show systematic differences in the PNS surface structure, with ALCAR models tending to have a more “fluffy” PNS surface or accretion disk around the PNS core. The specific angular momentum profiles and the field amplification in the PNS surface region are

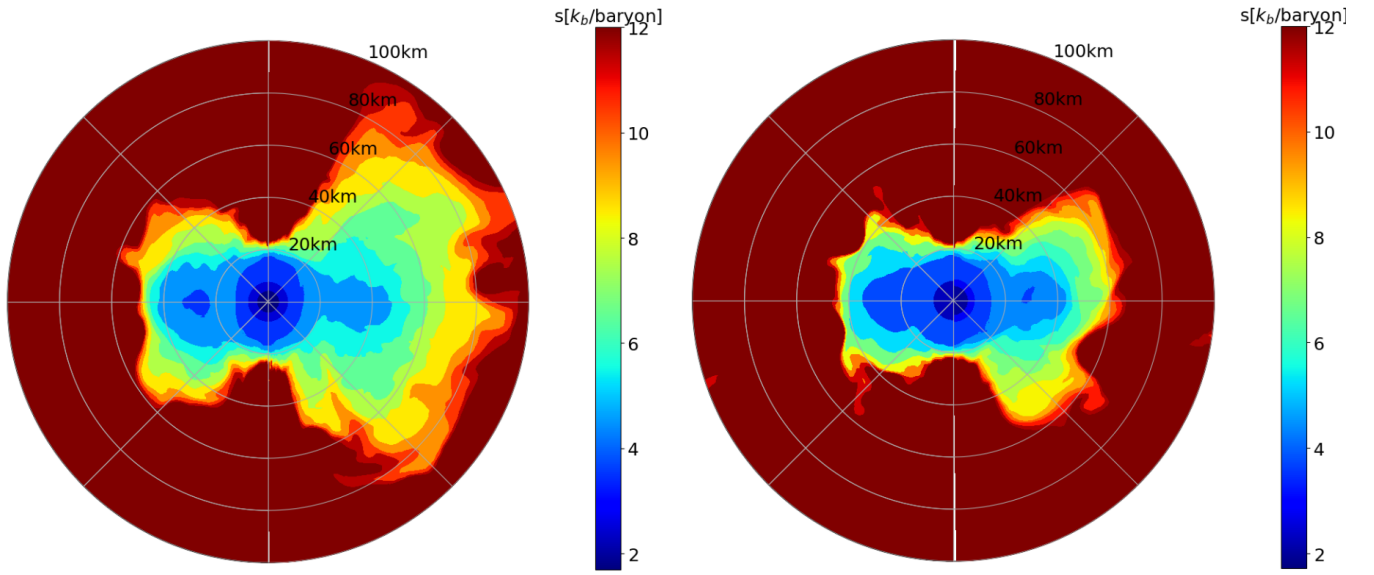


**Figure 18.** Left: 2D plots of the entropy  $s$  in the vicinity of the PNS for the standard-resolution model coco-HLLC-Rs (left half) and the high-resolution model coco-Res-Rs (right half) at  $\approx 0.46$  s. Right: Corresponding plot of the entropy  $s$  in model coco-HLLE-Rs (left half) and coco-HLLC-Rs (right half) at  $\approx 0.45$  s. The entropy in both plots is capped at  $12k_b/\text{baryon}$  to make the low-entropy, disk-like PNS surface region more clearly visible.

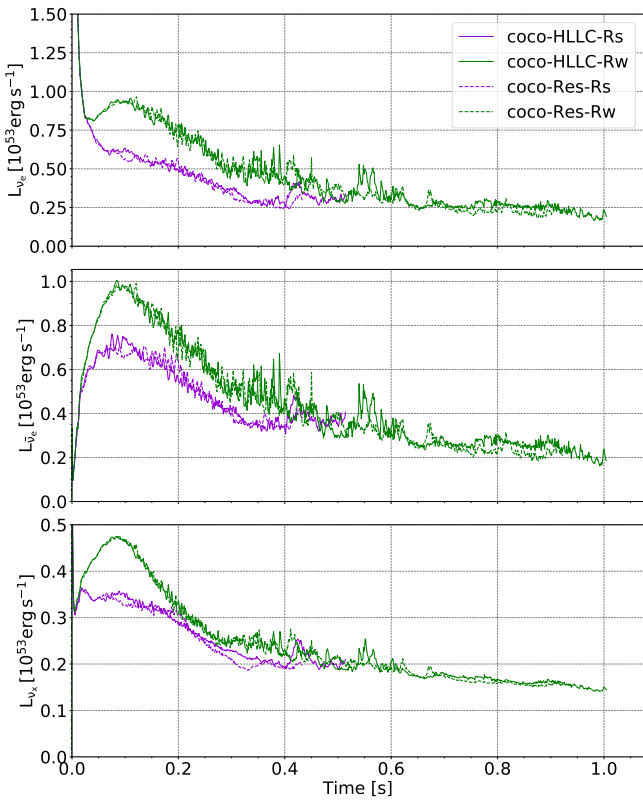


**Figure 19.** Comparison of the luminosities of electron neutrinos ( $\nu_e$ , top row), electron antineutrinos ( $\bar{\nu}_e$ , middle) and heavy-flavour neutrinos ( $\nu_x$ , bottom) for the standard-resolution coco-HLLC models and the high-resolution coco-Res models. Luminosities are measured as spherical averages at a radius of 2000 km.

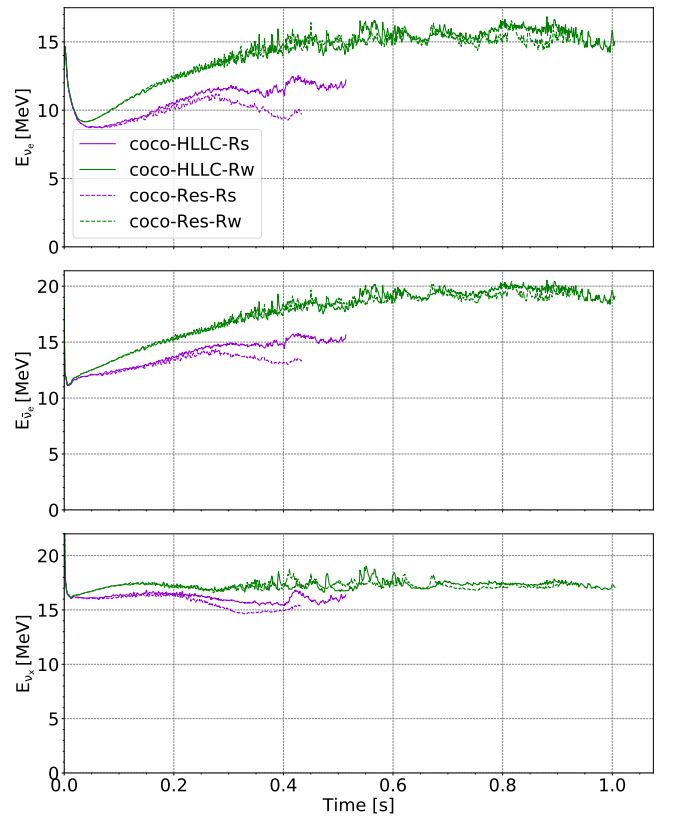


**Figure 20.** Comparison of the mean energies of electron neutrinos ( $\nu_e$ , top row), electron antineutrinos ( $\bar{\nu}_e$ , middle) and heavy-flavour neutrinos ( $\nu_x$ , bottom) for the standard-resolution coco-HLLC models and the high-resolution coco-Res models, measured as spherical averages at a radius of 2000 km.

also significantly different. The different PNS structure is reflected in the neutrino emission and explains the tendency towards smaller electron-flavour neutrino mean energies in *ALCAR*. However, difference in the neutrino emission also arise due to subtle differences in the infall dynamics and hence the mass accretion rate, and due to the disparate neutrino transport methodology.

We also compared the composition of the ejecta in the various models, specifically the distribution of the electron fraction  $Y_e$  as a crucial factor that decides, e.g., about the production of r-process material in MHD-driven supernovae. The *CoCoNuT* and *ALCAR* models are qualitatively in agreement in that they produce considerable neutron-rich material in the strong-field case and predominantly proton-rich material in the weak-field case. However, the width of the  $Y_e$ -distribution and the amount of very neutron-rich or very proton-rich material varies noticeably between *CoCoNuT* and *ALCAR*, and is also quite sensitive to the numerical resolution and the Riemann solver.

In contrast to 1D comparisons of supernova codes (Liebendörfer et al. 2005; Müller et al. 2010; O’Connor et al. 2018) and multi-D code comparisons for non-rotating, non-magnetised progenitors (Müller & Janka 2015; Cabezón et al. 2018; Just et al. 2018), disentangling and eliminating the causal factors behind discrepant results proves much more difficult. Therefore no attempt has been made to achieve perfect agreement between the two codes. It is perhaps rather astonishing that despite all the differences, the most coarse-grain metrics of the dynamics like the shock propagation and the explosion energy, and the  $Y_e$ -distribution still end up in qualitative agreement.

Our comparison study suggests that MHD supernova models in axisymmetry are quite sensitive to details of the numerical implementation, resolution, and the employed microphysics, and therefore still subject to significant uncertainties. While they appear robust on a qualitative level, there is clearly not the same level of convergence between codes that has been reached in 1D supernova simulations (Liebendörfer et al. 2005; Müller et al. 2010; O’Connor et al. 2018).

Of necessity, our work is only a first step in bracketing and reducing the uncertainties in MHD supernova models. Follow-up studies are highly desirable. Comparison studies with reduced model complexity, e.g., without neutrino transport in the post-bounce phase and an identical treatment of the collapse phase, may be useful to specifically identify and iron out differences between MHD solvers, rather than dealing with a coupled radiation MHD problem. Focusing on MHD only would also make it easier to conduct a comparison in 3D rather than in 2D, which will be critical to study aspects like dynamo field amplification and the kink instability in jet-driven explosions (Mösta et al. 2014; Kuroda et al. 2020). On the other hand, the impact of uncertainties in MHD supernova models with neutrino transport should also be explored in more depth. In particular, it would be desirable to investigate the implications for detailed nucleosynthesis yields rather than just considering the  $Y_e$ -distributions in our current study. While MHD supernova simulations still need to further mature in many respects, e.g., by considering more realistic initial magnetic field configurations (Varma & Müller 2021), further code comparisons will be an important tool on the long road towards a robust understanding of the role of magnetic fields in the explosions of massive stars.

## ACKNOWLEDGEMENTS

We thank A. Heger, D. Price and S. Campbell for useful discussions. BM acknowledges support by ARC Future Fellowship FT160100035.

MO acknowledges support from the Spanish Ministry of Science, Education and Universities (PGC2018-095984-B-I00) and the Valencian Community (PROMETEU/2019/071), the European Research Council under grant EUROPIUM-667912, and from the Deutsche Forschungsgemeinschaft (DFG, German Research Foundation) – Projektnummer 279384907 – SFB 1245 as well as from the Spanish Ministry of Science via the Ramón y Cajal programme (RYC2018-024938-I). Part of this work has been performed using computer time allocations from Astronomy Australia Limited’s ASTAC scheme, the National Computational Merit Allocation Scheme (NCMAS), and an Australasian Leadership computing grant on the NCI NF supercomputer Gadi. This research was supported by resources provided by the Pawsey Supercomputing Centre, with funding from the Australian Government and the Government of Western Australia.

## DATA AVAILABILITY

The data from our simulations will be made available upon reasonable requests made to the authors.

## REFERENCES

- Abdikamalov E., et al., 2015, *ApJ*, **808**, 70  
 Akiyama S., Wheeler J. C., Meier D. L., Lichtenstadt I., 2003, *ApJ*, **584**, 954  
 Aloy M. Á., Obergaulinger M., 2021, *MNRAS*, **500**, 4365  
 Baade W., Zwicky F., 1934, *Proceedings of the National Academy of Science*, **20**, 254  
 Balbus S. A., Hawley J. F., 1991, *ApJ*, **376**, 214  
 Bethe H. A., Wilson J. R., 1985, *ApJ*, **295**, 14  
 Bisnovatyi-Kogan G. S., Popov I. P., Samokhin A. A., 1976, *Ap&SS*, **41**, 287  
 Blondin J. M., Mezzacappa A., DeMarino C., 2003, *ApJ*, **584**, 971  
 Bugli M., Guilet J., Obergaulinger M., Cerdá-Durán P., Aloy M. A., 2020, *MNRAS*, **492**, 58  
 Bugli M., Guilet J., Obergaulinger M., 2021, *MNRAS*, **507**, 443  
 Buras R., Janka H. T., Rampp M., Kifonidis K., 2006, *A&A*, **457**, 281  
 Burrows A., 2013, *Reviews of Modern Physics*, **85**, 245  
 Burrows A., Hayes J., Fryxell B. A., 1995, *ApJ*, **450**, 830  
 Burrows A., Dessart L., Livne E., Ott C. D., Murphy J., 2007, *ApJ*, **664**, 416  
 Burrows A., Radice D., Vartanyan D., Nagakura H., Skinner M. A., Dolence J. C., 2020, *MNRAS*, **491**, 2715  
 Cabezón R. M., Pan K.-C., Liebendörfer M., Kuroda T., Ebinger K., Heinemann O., Perego A., Thielemann F.-K., 2018, *A&A*, **619**, A118  
 Cardall C. Y., Budiardja R. D., 2015, *ApJ*, **813**, L6  
 Chan C., Müller B., Heger A., 2020, *MNRAS*, **495**, 3751  
 Colella P., Sekora M. D., 2008, *Journal of Computational Physics*, **227**, 7069  
 Colella P., Woodward P. R., 1984, *Journal of Computational Physics*, **54**, 174  
 Colgate S. A., White R. H., 1966, *ApJ*, **143**, 626  
 Couch S. M., O’Connor E. P., 2014, *ApJ*, **785**, 123  
 Dedner A., Kemm F., Kröner D., Munz C. D., Schnitzer T., Wesenberg M., 2002, *Journal of Computational Physics*, **175**, 645  
 Dessart L., Burrows A., Livne E., Ott C. D., 2007, *ApJ*, **669**, 855  
 Eichler M., et al., 2018, *Journal of Physics G Nuclear Physics*, **45**, 014001  
 Einfeldt B., 1988, *SIAM Journal on Numerical Analysis*, **25**, 294  
 Evans C. R., Hawley J. F., 1988, *ApJ*, **332**, 659  
 Foglizzo T., Galletti P., Scheck L., Janka H. T., 2007, *ApJ*, **654**, 1006  
 Fröhlich C., et al., 2006, *ApJ*, **637**, 415  
 Grimmett J. J., Müller B., Heger A., Banerjee P., Obergaulinger M., 2021, *MNRAS*, **501**, 2764  
 Guilet J., Foglizzo T., 2012, *MNRAS*, **421**, 546  
 Guilet J., Müller E., 2015, *MNRAS*, **450**, 2153  
 Guilet J., Müller E., Janka H.-T., 2015, *MNRAS*, **447**, 3992  
 Gurski K., 2001, in *APS Meeting Abstracts*. p. D2.007  
 Halevi G., Mösta P., 2018, *MNRAS*, **477**, 2366  
 Handy T., Plewa T., Odrzywołek A., 2014, *ApJ*, **783**, 125

- Hanke F., Müller B., Wongwathanarat A., Marek A., Janka H.-T., 2013, *ApJ*, **770**, 66
- Hartmann D., Woosley S. E., El Eid M. F., 1985, *ApJ*, **297**, 837
- Heger A., Langer N., Woosley S. E., 2000, *ApJ*, **528**, 368
- Heger A., Woosley S. E., Spruit H. C., 2005, *ApJ*, **626**, 350
- Herant M., 1995, *Space Sci. Rev.*, **74**, 335
- Horowitz C. J., 2002, *Phys. Rev. D*, **65**, 043001
- Horowitz C. J., Caballero O. L., Lin Z., O'Connor E., Schwenk A., 2017, *Phys. Rev. C*, **95**, 025801
- Hüdepohl L., 2014, PhD thesis, Technical University of Munich, <https://mediatum.ub.tum.de/1177481>
- Janka H.-T., 2012, *Annual Review of Nuclear and PARTICLE Science*, **62**, 407
- Jardine R., Powell J., Müller B., 2021, Gravitational Wave Signals from Two-Dimensional Core-Collapse Supernova Models with Rotation and Magnetic Fields ([arXiv:2105.01315](https://arxiv.org/abs/2105.01315))
- Just O., Obergaulinger M., Janka H. T., 2015, *MNRAS*, **453**, 3386
- Just O., Bollig R., Janka H. T., Obergaulinger M., Glas R., Nagataki S., 2018, *MNRAS*, **481**, 4786
- Kobayashi C., Karakas A. I., Lugaro M., 2020, *ApJ*, **900**, 179
- Kotake K., Sawai H., Yamada S., Sato K., 2004, *ApJ*, **608**, 391
- Kuroda T., Arcones A., Takiwaki T., Kotake K., 2020, *ApJ*, **896**, 102
- Lattimer J. M., Swesty D. F., 1991, *Nuclear Phys. A*, **535**, 331
- LeBlanc J. M., Wilson J. R., 1970, *ApJ*, **161**, 541
- Liebendörfer M., 2005, *ApJ*, **633**, 1042
- Liebendörfer M., Rampp M., Janka H. T., Mezzacappa A., 2005, *ApJ*, **620**, 840
- Marek A., Dimmelmeier H., Janka H. T., Müller E., Buras R., 2006, *A&A*, **445**, 273
- Martínez-Pinedo G., Fischer T., Lohs A., Huther L., 2012, *Phys. Rev. Lett.*, **109**, 251104
- Masada Y., Takiwaki T., Kotake K., 2015, *ApJ*, **798**, L22
- McNeill L. O., Müller B., 2021, Differential Rotation in a 3D Simulation of Oxygen Shell Burning ([arXiv:2107.00173](https://arxiv.org/abs/2107.00173))
- Meier D. L., Epstein R. I., Arnett W. D., Schramm D. N., 1976, *ApJ*, **204**, 869
- Melson T., Kresse D., Janka H.-T., 2020, *ApJ*, **891**, 27
- Mezzacappa A., Endeve E., Messer O. E. B., Bruenn S. W., 2020, *Living Reviews in Computational Astrophysics*, **6**, 4
- Miyoshi T., Kusano K., 2005, *Journal of Computational Physics*, **208**, 315
- Moiseenko S. G., Bisnovatyi-Kogan G. S., Ardeljan N. V., 2006, *MNRAS*, **370**, 501
- Mösta P., et al., 2014, *ApJ*, **785**, L29
- Mösta P., Ott C. D., Radice D., Roberts L. F., Schnetter E., Haas R., 2015, *Nature*, **528**, 376
- Mösta P., Roberts L. F., Halevi G., Ott C. D., Lippuner J., Haas R., Schnetter E., 2018, *ApJ*, **864**, 171
- Müller B., 2009, PhD thesis, Technische Universität München
- Müller B., 2015, *MNRAS*, **453**, 287
- Müller B., 2016, *Publ. Astron. Soc. Australia*, **33**, e048
- Müller B., 2020, *Living Reviews in Computational Astrophysics*, **6**, 3
- Müller E., Hillebrandt W., 1979, *A&A*, **80**, 147
- Müller B., Janka H. T., 2015, *MNRAS*, **448**, 2141
- Müller B., Varma V., 2020, *MNRAS*, **498**, L109
- Müller B., Janka H.-T., Dimmelmeier H., 2010, *ApJS*, **189**, 104
- Müller B., Janka H.-T., Heger A., 2012, *ApJ*, **761**, 72
- Müller B., et al., 2019, *MNRAS*, **484**, 3307
- Nagakura H., Burrows A., Radice D., Vartanyan D., 2019, *MNRAS*, **490**, 4622
- Nishimura N., Takiwaki T., Thielemann F.-K., 2015, *ApJ*, **810**, 109
- O'Connor E., et al., 2018, *Journal of Physics G Nuclear Physics*, **45**, 104001
- Obergaulinger M., 2008, PhD thesis, Technische Universität München, <https://mediatum.ub.tum.de/doc/632729/632729.pdf>
- Obergaulinger M., Aloy M. Á., 2017, *MNRAS*, **469**, L43
- Obergaulinger M., Aloy M. Á., 2020, *MNRAS*, **492**, 4613
- Obergaulinger M., Aloy M. Á., 2021, *MNRAS*, **503**, 4942
- Obergaulinger M., Aloy M. A., Müller E., 2006, *A&A*, **450**, 1107
- Obergaulinger M., Cerdá-Durán P., Müller E., Aloy M. A., 2009, *A&A*, **498**, 241
- Obergaulinger M., Janka H. T., Aloy M. A., 2014, *MNRAS*, **445**, 3169
- Obergaulinger M., Just O., Aloy M. A., 2018, *Journal of Physics G Nuclear Physics*, **45**, 084001
- Ott C. D., Burrows A., Dessart L., Livne E., 2008, *ApJ*, **685**, 1069
- Powell J., Müller B., Heger A., 2021, *MNRAS*, **503**, 2108
- Price D. J., 2008, *Journal of Computational Physics*, **227**, 10040
- Pruet J., Hoffman R. D., Woosley S. E., Janka H. T., Buras R., 2006, *ApJ*, **644**, 1028
- Radice D., Ott C. D., Abdikamalov E., Couch S. M., Haas R., Schnetter E., 2016, *ApJ*, **820**, 76
- Raynaud R., Guilet J., Janka H.-T., Gastine T., 2020, *Science Advances*, **6**, eaay2732
- Reboul-Salze A., Guilet J., Raynaud R., Bugli M., 2021, *A&A*, **645**, A109
- Reichert M., Obergaulinger M., Eichler M., Aloy M. Á., Arcones A., 2021, *MNRAS*, **501**, 5733
- Rembiasz T., Obergaulinger M., Cerdá-Durán P., Müller E., Aloy M. A., 2016a, *MNRAS*, **456**, 3782
- Rembiasz T., Guilet J., Obergaulinger M., Cerdá-Durán P., Aloy M. A., Müller E., 2016b, *MNRAS*, **460**, 3316
- Richers S., Nagakura H., Ott C. D., Dolence J., Sumiyoshi K., Yamada S., 2017, *ApJ*, **847**, 133
- Sawai H., Yamada S., 2016, *ApJ*, **817**, 153
- Sawai H., Kotake K., Yamada S., 2005, *ApJ*, **631**, 446
- Sawai H., Yamada S., Suzuki H., 2013, *ApJ*, **770**, L19
- Scheck L., Janka H. T., Foglizzo T., Kifonidis K., 2008, *A&A*, **477**, 931
- Shankar S., Mösta P., Barnes J., Duffell P. C., Kasen D., 2021, Protomagnetar jets as central engines for broad-lined type Ic supernovae ([arXiv:2105.08092](https://arxiv.org/abs/2105.08092))
- Spruit H. C., 2002, *A&A*, **381**, 923
- Suresh A., Huynh H. T., 1997, *Journal of Computational Physics*, **136**, 83
- Suwa Y., Takiwaki T., Kotake K., Sato K., 2007, *PASJ*, **59**, 771
- Takiwaki T., Kotake K., Nagataki S., Sato K., 2004, *ApJ*, **616**, 1086
- Takiwaki T., Kotake K., Sato K., 2009, *ApJ*, **691**, 1360
- Thompson C., Duncan R. C., 1993, *ApJ*, **408**, 194
- Tricco T. S., Price D. J., Bate M. R., 2016, *Journal of Computational Physics*, **322**, 326
- Varma V., Müller B., 2021, *MNRAS*, **504**, 636
- Wanajo S., Janka H.-T., Müller B., 2011, *ApJ*, **726**, L15
- Wanajo S., Müller B., Janka H.-T., Heger A., 2018, *ApJ*, **852**, 40
- Winteler C., Käppeli R., Perego A., Arcones A., Vasset N., Nishimura N., Liebendörfer M., Thielemann F. K., 2012, *ApJ*, **750**, L22
- Woosley S. E., Bloom J. S., 2006, *ARA&A*, **44**, 507
- Woosley S. E., Heger A., 2006, *ApJ*, **637**, 914
- Yamada S., Janka H.-T., Suzuki H., 1999, *A&A*, **344**, 533
- Yoshida T., Takiwaki T., Aguilera-Dena D. R., Kotake K., Takahashi K., Nakamura K., Umeda H., Langer N., 2021, *MNRAS*, **506**, L20

This paper has been typeset from a  $\text{\TeX}/\text{\LaTeX}$  file prepared by the author.